ANL/FE-93/1

Corrosion Performance of Materials for Advanced Combustion Systems

by K. Natesan, M. Yanez-Herrero, and C. Fornasieri

Argonne National Laboratory, Argonne, Illinois 60439
operated by The University of Chicago
for the United States Department of Energy under Contract W-31-109-Eng-38

Argonne National Laboratory, with facilities in the states of Illinois and Idaho, is owned by the United States government, and operated by The University of Chicago under the provisions of a contract with the Department of Energy.

Reproduced from the best available copy.

Available to DOE and DOE contractors from the
Office of Scientific and Technical Information
P.O. Box 62
Oak Ridge, TN 37831
Prices available from (615) 576-8401

Available to the public from the
National Technical Information Service
U.S. Department of Commerce
5285 Port Royal Road
Springfield, VA 22161

Distribution Category:
Coal-Based Materials
and Components (UC-114)

ARGONNE NATIONAL LABORATORY
9700 South Cass Avenue, Argonne, Illinois 60439

ANL/FE-93/1

CORROSION PERFORMANCE OF MATERIALS FOR ADVANCED COMBUSTION SYSTEMS

by

K. Natesan, M. Yanez-Herrero, and C. Fornasieri

Energy Technology Division

December 1993

Work sponsored by

U.S. DEPARTMENT OF ENERGY
Pittsburgh Energy Technology Center and Office of Fossil Energy,
Advanced Research and Technology Development Materials Program,
under Contract W-31-109-Eng-38.

CONTENTS

FIGURES

TABLES

CORROSION PERFORMANCE OF MATERIALS FOR ADVANCED COMBUSTION SYSTEMS

by

K. Natesan, M. Yanez-Herrero, and C. Fornasieri

ABSTRACT

Conceptual designs of advanced combustion systems that utilize coal as a feedstock require high-temperature furnaces and heat transfer surfaces capable of operating at more elevated temperatures than those prevalent in current coal-fired power plants. The combination of elevated temperatures and hostile combustion environments necessitates development/application of advanced ceramic materials in these designs. The present report characterizes the chemistry of coal-fired combustion environments over the wide temperature range that is of interest in these systems and discusses preliminary experimental results on several materials with potential for application in these systems.

INTRODUCTION

The production of clean liquid and gaseous fuels from coal offers a means of reducing U.S. dependence on imported oil while using our vast coal reserves in an efficient and environmentally acceptable manner. A significant reserve of high-sulfur coal is available for energy use, provided it can be cleaned, before or during conversion, to meet federal emission standards for SO_2. Coal is a complex and relatively dirty fuel that contains varying amounts of sulfur and a substantial fraction of noncombustible mineral constituents, commonly called ash. An examination of the use of fossil fuels in the generation of electric power (see Fig. 1) shows that coal use in this sector grew dramatically from 1978 to 1986, after which it stabilized at ≈80%. The consumption of natural gas and crude oil in the power sector declined during the same period, to ≈14 and 6%, respectively.[1] Further gains (as a percentage) for coal in this sector are considered unlikely in view of the more stringent environmental regulations for power plants, and the logistics of those plants that necessitate the use of gas or oil as a feedstock. Even though the relative percent of coal consumption will not change significantly, the tonnage usage of coal is expected to increase with an increase in the demand for electricity.

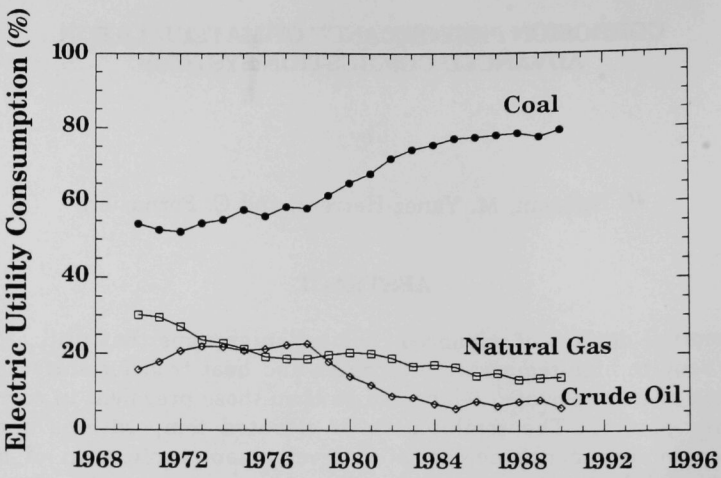

Fig. 1. Fossil fuel consumption for electric power production, 1970–1990

In recent years, extensive deliberations have been held in public forums and policy meetings on global warming, CO_2 generation, acid rain, more stringent New Source Performance Standards (NSPS), and environmental compliance, as well as the role of effluents from fossil-fired power plants in all of the above. It is evident that electric utilities are concerned with these deliberations and their effects on utility use of different coal feedstocks. Especially vulnerable are utilities that use high-sulfur coal from eastern U.S. With current and future legislation and anticipated stricter emission standards, it is imperative that deployment of systems with higher thermal efficiency and lower environmental impact will be the norm of the future. In addition to coal gasification combined-cycle systems, and retrofits of open-cycle magnetohydrodynamic topping cycles, the U.S. Department of Energy has embarked on programs to develop coal-fired boilers with advanced steam cycles, fluidized-bed combustion cogeneration systems, a high-performance power system (HIPPS), and a low-emission boiler system (LEBS).

BACKGROUND

The HIPPS, shown in Fig. 2, would employ a cycle that combines a gas turbine driven by a working fluid (air), separately heated in a high-temperature advanced furnace, and conventional steam turbines.[2] The ultimate goal is to produce electricity from coal with an overall thermal efficiency of 47% or higher

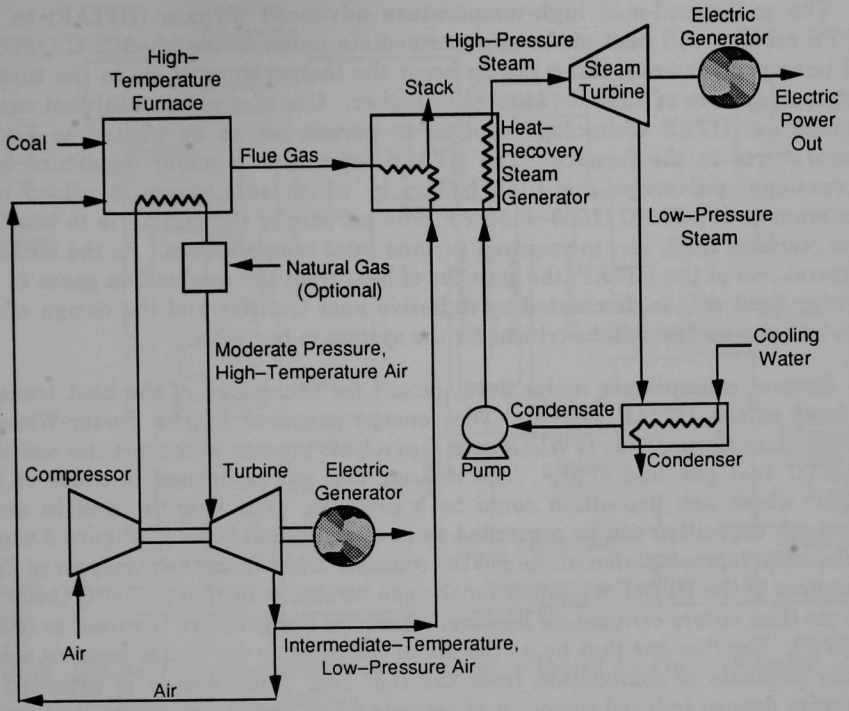

Fig. 2. Schematic representation of a high–performance power system

(compared with ≈35% for current systems) and to reduce carbon dioxide (CO_2) emissions by 25-30%. The targeted requirements for a HIPPS are

- a minimum conversion efficiency, coal to busbar, of 47%;
- NO_x < 0.15 lb (as NO_2) per million Btu of fuel input;
- SO_x < 0.15 lb (as SO_2) per million Btu of fuel input;
- particulates < 0.0075 lb per million Btu of fuel input;
- benign solid waste streams;
- initial fueling with coal and natural gas, with coal providing at least 65% of heat input and ultimately 95%;

and

- commercial plants with a 65% annual capacity factor and capability to generate electricity at a 10% lower cost.

The pulverized-coal high-temperature advanced furnace (HITAF) in the HIPPS concept will heat air to an intermediate temperature of ≈982°C (1800°F) and burn supplemental clean fuel to boost the temperature of air to the turbine inlet temperature of 1316°C (2400°F) or higher. Use of supplemental fuel can be reduced as HITAF technology evolves to permit air to be heated to higher temperatures in the furnace. The HITAF represents a major departure from conventional pulverized-coal-fired boilers in which only steam is raised to a maximum of 538-621°C (1000–1150°F). The purpose of the HITAF is to heat the clean working fluid, air, to required turbine inlet temperatures. At the elevated temperatures of the HITAF, the transfer of heat from the combustion gases to the working fluid will be dominated by radiative heat transfer and the design of the heat transfer surface will be critical for the system to be viable.

Several concepts are under development for the design of the heat transfer surfaces in the HITAF system. The concept proposed by the Foster-Wheeler Development Corporation (FWDC) uses a pyrolysis process to convert the coal into low-BTU fuel gas and char.[3] The cleaned fuel gas is burned in areas of the HITAF where ash deposition could be a problem. The char is fired in areas where ash deposition can be controlled as in conventional boilers. Figure 3 shows a schematic representation of the FWDC concept. Char from the pyrolyzer is fired in an area of the HITAF where air for the gas turbine is heated to 760°C (1400°F). The air then enters ceramic air heaters, where the temperature is raised to 982°C (1800°F). The flue gas that heats the air in the ceramic air heater consists solely of the products of combustion from the fuel gas. This design is expected to minimize deposit-induced corrosion of ceramic tubes and stress effects that would arise from sootblowing. The approach requires that the flue gas be cleaned by hot-gas filter techniques to prevent alkali corrosion and particulate erosion of the ceramic tubes. In this concept, air with a 1316°C (2400°F) turbine inlet temperature is achieved by supplemental firing with natural gas in a gas turbine combustor.

The concept proposed by United Technologies Research Center (UTRC) involves a combustor with a controlled fuel distribution/long axial flame in which the heat release is stretched out, allowing for progressive heat removal.[4] The compressed air is heated to 704°C (1300°F) in a convective air heater and then in a radiative air heater to 982°C (1800°F). A schematic representation of the radiant air heater is shown in Fig. 4. A protective layer of refractory is provided on the fire side of the radiant air heater to prevent corrosion of air passages by ash and slag that inevitably will deposit on the heat transfer surface. This concept also involves heating of the air with supplemental natural gas firing to achieve a 1316°C (2400°F) turbine inlet temperature.

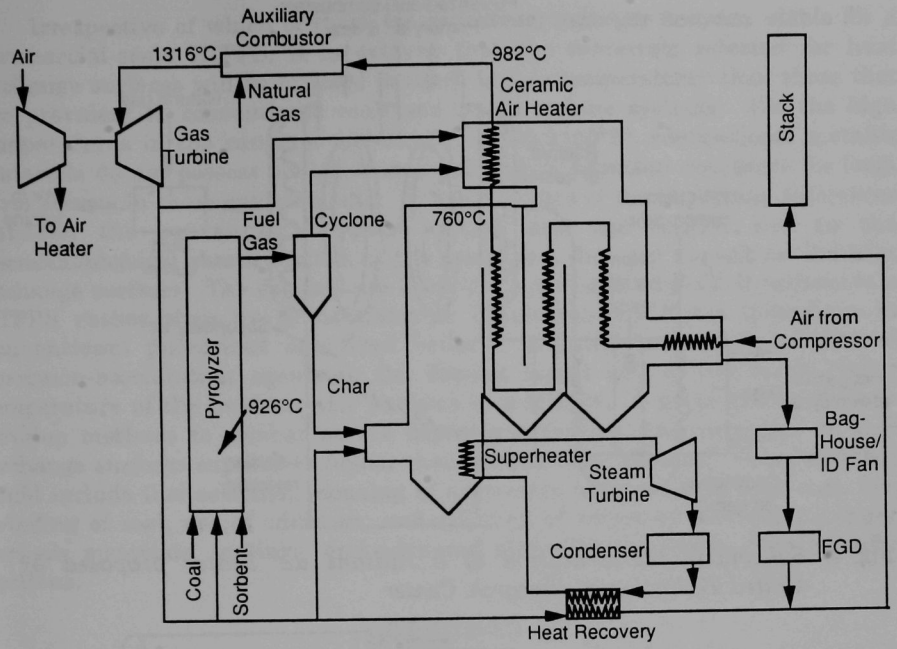

Fig. 3. Schematic representation of a concept proposed by Foster–Wheeler Development Corporation

The concept proposed by Argonne National Laboratory (ANL) involves an air-wall heat exchanger design that utilizes radiation rather than convection as the principal mode of heat transfer.[5] Depending on combustion gas and surface temperatures, the heat transfer coefficient for radiation can be 200-400 $W/m^2 K$ compared with 50-100 $W/m^2 K$ obtainable with convective cross-flow heat exchangers. A method has been proposed to improve the heat transfer coefficient of the tube side (which carries the working fluid air) by uniform dispersion of thin filaments inside the tube. The filaments are heated radiatively by the tube surface and, in turn, transfer the heat convectively to the flowing air. The filaments are nearly isothermal with air by virtue of a high heat transfer coefficient and extended surface area obtained with thin filaments. Calculations showed that tube-side heat transfer coefficients in the range of 500-1100 $W/m^2 K$ can be obtained with the filaments. In addition, transpiration of air (from the tube side to the fire side) through porous walls is proposed as a means to minimize deposition of combustion products on the air-wall surfaces. Figure 5 shows a schematic representation of a wall design with a two-stage, two-stream configuration of air walls for heating air from 627°C (1160°F) to 1260°C (2300°F).

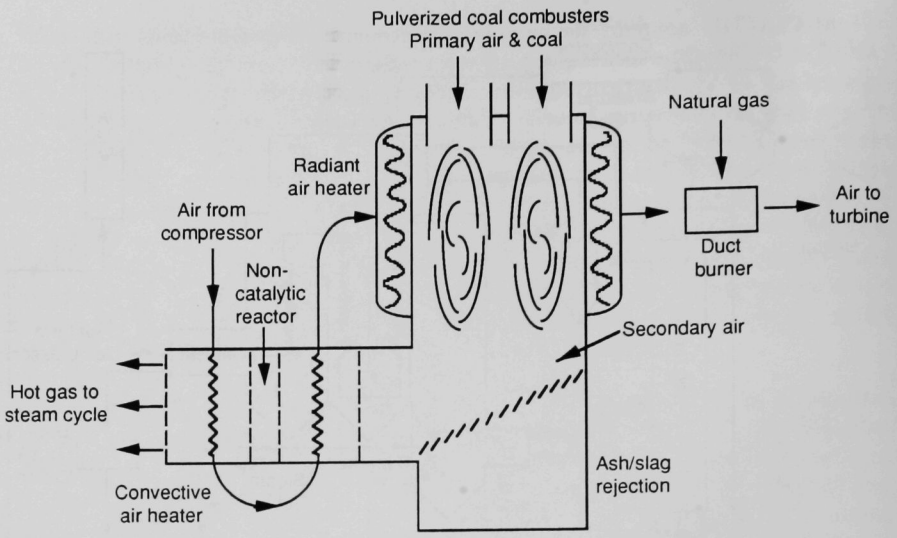

Fig. 4. Schematic representation of a radiant air heater proposed by United Technologies Research Center

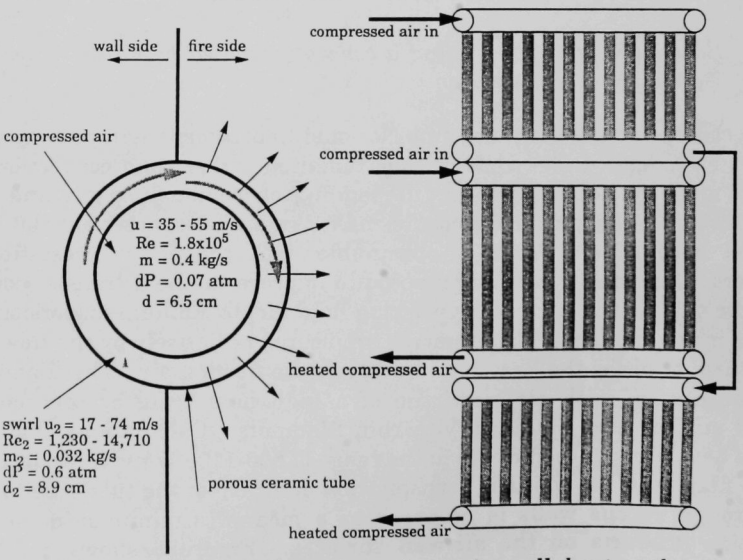

Fig. 5. Schematic representation of an air–wall heat exchanger proposed by Argonne National Laboratory

Irrespective of which of these (or any other) concepts becomes viable for a commercial-scale HIPPS, it is evident that the materials selected for heat exchange surfaces will be exposed to much higher temperatures than those that are prevalent in conventional coal-fired steam-turbine systems. For the high temperatures in the range of 982-1316°C (1800-2400°F), conventional metallic materials do not possess adequate strength and/or corrosion resistance for long-term service in these environments. In addition, one of the important differences between the conventional boiler system and the HIPPS lies in the chemical/physical characteristics of the ash layers that can deposit on the heat exchange surfaces. The deposits are likely to be dominated by alkali sulfates in a HIPPS rather than by pyrosulfates or alkali-iron-trisulfates (prevalent in conventional pulverized coal-fired boilers), and the increased mobility of corrosion-accelerating agents in the deposit layers due to the much higher temperature of the heat-transfer surfaces in a HIPPS. A major challenge is to develop methods to combat severe deposition, erosion, and corrosion of heat exchange surfaces exposed to higher than normal temperatures. These methods could include fuel selection, cleaning of aggressive contaminants from coal, fine grinding of coal, use of additives, and selection of advanced corrosion-resistant ceramic materials, coatings, and advanced alloys for vulnerable heat transfer sections.

OBJECTIVES

The objectives of the present program are to (a) evaluate the chemistry of gaseous and condensed products that arise in combustion of coal and (b) evaluate candidate materials for application in high-temperature advanced furnaces (HITAFs) for the HIPPS concept. The chemistry calculations involve determination of type and amount of combustion products over the wide temperature range of 700-1700°C (1212-3092°F) at 1 atm pressure. In addition, nonequilibrium conditions due to kinetic factors are incorporated to assess their influence on the chemistry of deposition environments. The experimental work on the candidate materials involves procurement of materials that include highly alloyed metallic alloys, monolithic ceramic materials, metal-matrix ceramic composites and ceramic-matrix ceramic composites, and laboratory testing of these materials in air and in simulated combustion atmospheres. Salt and ash/slag mixtures are included in the study for evaluation of deposit effects on corrosion processes. Another objective is to characterize, by scanning electron microscopy, X-ray diffraction, and electron-probe microanalysis, the microstructures of the candidate materials before exposure and after testing. The ultimate goal of the program is to assess the materials from the standpoint of corrosion performance, mechanical integrity, microstructural stablity, and long-term durability for application in heat transfer surfaces in HIPPS.

COMBUSTION CHEMISTRY

The overall chemistry of coal-conversion processes will be influenced by (a) thermodynamic factors, (b) kinetic factors, and (c) interactions between kinetic and thermodynamic factors. The thermodynamic factors are the nature and mass of elements present in coal, coal/oxidant ratio, temperature, pressure in the reaction chamber, etc. Among factors controlling the kinetics are reaction rates of key chemical reactions, reactor configuration and geometry, and the hydrodynamic conditions that influence the transport of reaction species. Moreover, some kinetic factors affecting mass transfer of reactants and products, as well as reaction rates of key chemical reactions, can affect thermodynamic driving forces. For example, slow reactions of some constituents could lead to higher chemical potentials in those constituents than would be present at equilibrium and could lead to different reaction products than are possible at equilbrium. Ideally, characterization of final products in coal-conversion processes should consider all of these factors.

An ideal beginning for solving such a complex problem is to evaluate the thermodynamic factors first. Because the equilibrium-reaction products can be calculated as a function of temperature and pressure for a given composition of coal and feed materials, key chemical reactions that produce these reaction products can be identified. A knowledge of such key reactions is required to evaluate the effects of the kinetic factors related to these key reactions. Effects of other system-dependent kinetic factors involving reactor geometry and hydrodynamics of reacting species, which may be evaluated if the specifics of the reactor system are known, will also require knowledge of the kinetics of rate-controlling chemical reactions. Calculations of the chemistry of coal-conversion products are complicated by the presence of as many as 15 elements in the feed materials. Several hundred species, including multiple solution phases, are thermodynamically feasible under coal-conversion conditions. Extensive calculations of coal combustion chemistry have been performed earlier.[6] The goal of the present calculations is to derive a complete characterization of combustion products as a function of key thermodynamic factors that are relevant to HIPPSs and identify important chemical reactions that can occur from the standpoint of materials interactions.

Calculational Approach

The computer program used for the computations is based on calculating the equilibrium concentrations of various species by minimizing the free energy of the system.[7] The minimization problem is usually expressed by the following equation:

$$\text{Minimize } G = \sum_{l}\sum_{i} N_{il}\,\mu_{il} \tag{1}$$

subject to the following constraints

$$b_j = \sum_{l}\sum_{i} a_{ij} N_{il} \tag{2}$$

$$N_{il} \geq 0, \tag{3}$$

where i, j, and l denote species, elements, and phases, respectively; N_{il} and μ_{il} are the moles and chemical potential of the i'th species in the l'th phase, respectively; a_{ij} is the stoichiometric coefficient of the j'th element in the i'th species; b_j is the total number of moles of the j'th element in the given chemical system. The right side of Eq. 1 is a nonlinear function of the concentration of each of the species i in the l'th phase, whereas the mass balance constraint expressed in Eq. 2 is linear. We thus have a nonlinear optimization problem with linear constraints. Equation 3 guarantees that the concentration of any species in any phase is non-negative.

Various algorithms are available for solving chemical equilibrium problems based on direct solution of the nonlinear optimization problem (Eqs. 1-3). The principal difficulty with this approach is that trace concentrations cannot be determined accurately because they have little effect on the mass balance constraints (Eq. 2) or on the Gibbs free energy function (Eq. 1). In addition, nonlinearity leads to singularities and problems with convergence, especially for large systems. Because of the special structure of the free energy function (Eq. 1), the concept of geometric programming may be used to transform the minimization problem (Eqs. 1-3) to a primal geometric problem.[7,8] The solution of the primal geometric problem results in equilibrium concentrations of all the species in all the phases.

Thermodynamic Data Base

The calculational program is linked to a critically analyzed data base that consists of the thermodynamic properties of ≈1800 species.[9] Thermodynamic data in the data base are stored as a set of 14 coefficients, seven each for two temperature ranges: (a) 27-727°C (80-1340°F) and (b) above 727°C (1340°F). The two sets of coefficients are constrained to yield identical results at the crossover temperature of 727°C (1340°F). These seven (a_1,....., a_7) coefficients are represented in the following three equations:

$$C_p/R = a_1 + a_2T + a_3T^2 + a_4T^3 + a_5T^4 \tag{4}$$

$$H_T/RT = 1/T\left(\int \frac{C_p}{R}\,dT + a_6\right) \tag{5}$$

$$S_T/R = \int \frac{C_p}{RT}\,dT + a_7 \tag{6}$$

where C_p, H_T, and S_T are the heat capacity, enthalpy, and entropy at temperature T, respectively; and R is the ideal gas constant.

For a given substance, coefficients a_1, ..., a_7 are generated by simultaneous least square fits of heat capacity, entropy, and enthalpy data. Major sources of these data for generating the temperature coefficients are the JANAF thermochemical tables and other compilations.[10-13] Data for a small number of relevant species not available in these sources have also been generated from other sources and have been added to the existing data base.

Input and Output

The input and output of the computer program are similar to those of the NASA computer program for calculating chemical equilibria.[14,15] The amount of reactants may be supplied in mass or mole units. For input, the program requires the components of the solution phase(s) and the corresponding stoichiometric coefficients of these components. The program is set to handle up to 300 species and contains the option to omit certain species that do not form because of kinetic factors. This option leads to a convenient way to simulate a user-defined nonequilibrium condition due to a kinetic constraint. In a given case, an additional 450 species, which are known not to form (e.g., calcium under oxidizing conditions), may be omitted. The current program assumes an ideal solution, but can be augmented to perform calculations for nonideal solutions as well. Thermodynamic data of the species relevant to a given problem need not be supplied as input, because the program is linked to the thermodynamic data base described earlier. The program identifies all of the species in the data base that contain the elements (carbon, hydrogen, etc.) in the given problem. A minimization of the total free energy of the system leads to identification of appropriate (up to 300) species that are stable. The major advantage of this program is its unique method of linearizing the equation for the free energy minimization. The program yields a robust method for performing such computations for the stable species and their relative concentrations.

Calculation Plan

An Illinois bituminous coal containing 3.41 wt.% sulfur was chosen for the present analysis. To evaluate the effect of a lower sulfur content, we also considered a second composition with a sulfur content of 1 wt.% and all other constituents in the same proportions as the first. The composition of the coal used in the calculations is shown in Table 1. The theoretical oxygen requirement for combustion is the amount of oxygen required to convert the carbon, sulfur, and hydrogen to carbon dioxide, sulfur dioxide, and water, respectively, less the free oxygen present in coal. Oxygen as dry air (77 wt.% N_2 and 23 wt.% O_2) is used for the coal-conversion process. The stoichiometric ratio of oxygen (SRO) is defined as the ratio of the actual amount of oxygen used for conversion of coal to the oxygen required for complete oxidation. For the present calculation, 12 elements can be identified and there are more than 300 compounds in the temperature range of 727-1727°C (1340-3140°F). A list of 252 species considered for the present calculations is shown in Table 2. An additional 66 species, which are likely to be present in insignificant amounts under the present conditions, are not considered in the calculations. In the present report, oxidizing conditions are defined as cases where the SRO is equal to, or greater than, 1.0 (i.e., oxygen supplied for the coal conversion is equal to, or more than, that needed for complete oxidation). In the calculations, the SRO is varied from 1.0 to 1.3 for oxidizing conditions typical of coal combustion systems. The total pressure of the system is maintained at 1 atm for all the calculations.

Table 1. Composition of high-sulfur coal used in the present work

Coal Constituents		Ash Constituents	
Species	Wt.%	Species	Wt.%
C	60.15	SiO_2	46.77
H	4.26	Fe_2O_3	16.22
N	0.97	Al_2O_3	18.47
S	3.41	CaO	6.91
Cl	0.05	MgO	1.28
H_2O	10.54	SO_3	4.35
O	7.30	Na_2O	4.96
Ash	13.32	Unknown	1.04
Total	100.00		100.00

Table 2. Selected species considered for the present calculations

The Following 252 Species are Being Considered in This System:

AL(S)	AL(G)	ALCL(G)	ALCLO(S)	ALCLO(G)	ALCL2(G)	ALCL3(S)
ALCL3(L)	ALCL3(G)	ALCL4NA(S)	ALCL6NA3(S)	ALHO(G)	ALHO2(G)	ALN(S)
ALNAO2(S)	ALO(G)	ALO2(G)	ALS(G)	AL2(G)	AL2CA06SI(S)	AL2CA207SI(S)
AL2CA306(S)	AL2CA3012SI3(S)	AL2CL6(G)	AL2FE04(S)	AL2MG04(S)	AL2MG04(L)	AL2NA2012SI4(S)
AL2NA2016SI8(S)	AL2NA04(S)	AL20(G)	AL202(G)	AL203(S),ALP	AL203(S),GAM	AL203(S),DEL
AL203(S),KAP	AL203(L)	AL205SI(S),SILL	AL205SI(S),ANDA	AL205SI(S),KYAN	AL207SI2(S)	AL2012S3(S)
AL2S3(S)	AL4MG2018SI5(S)	AL4C3(S)	AL6013SI2(S)	C(S)	CCA03(S)	CCL(G)
CCLH(G)	CCLO(G)	CCL4(G)	CFE3(S)	CH(G)	CHN(G)	CHNO(G)
CHO(G)	CH2(G)	CH20(G)	CH3(G)	CH4(G)	C2H6(G)	C8H16(G)
CN(G)	CNNA(S)	CNNA(L)	CNNA(G)	CNO(G)	CN2(G)	CNA203(S)
CNA203(L)	CO(G)	COS(G)	CO2(G)	CS(G)	CSI(S),ALPHA	CSI(S),BETA
C2H2(G)	C2H4(G)	C2MG(S)	C3MG2(S)	C6FE06(G)	CA(S),ALPHA	CA(S),BETA
CA(L)	CACL(G)	CACL2(S)	CACL2(L)	CACL2(G)	CAFE204(S)	CAHO(G)
CAH202(G)	CAMGO2(S)	CAMGO4SI(S)	CAO(S)	CAO(L)	CAO(G)	CAO3S(S)
CAO3SI(S)	CAO3SI(L)	CAO4S(S)	CA2FE206(S)	CA2MGO7SI2(S)	O3S(G)	CA306SI(S)
CA307SI2(S)	CAS(S)	CAS(G)	CL(G)	CLFE(G)	CLH(G)	CLHO(G)
CLH3SI(G)	CLH4N(S)	CLMG(G)	CLNO(G)	CLNO2(G)	CLNA(S)	CLNA(L)
CLNA(G)	CLNAO4(S)	CLO(G)	CLO2(G)	CLS2(G)	CLSI(G)	CL2FE(S)
CL2FE(L)	CL2FE(G)	CL2H2SI(G)	CL2MG(S)	CL2MG(L)	CL2MG(G)	CL2NA2(G)
CL20(G)	CL202S(G)	CL2S(G)	CL2S2(G)	CL2SI(G)	CL2(G)	CL3FE(S)
CL3FE(L)	CL3FE(G)	CL3HSI(G)	CL4FE2(G)	CL4MG2(G)	CL6FE2(G)	FE(S),ALPHA
FE(S),GAMMA	FE(L)	FE(G)	FEH202(S)	FEH202(G)	FEH303(S)	FE2NA204(S)
FE0.9470(S)	FEO(S)	FEO(L)	FEO(G)	FEO3SI(L)	FEO4S(S)	FE.877S(S),PYRR
FES(S)	FES(L)	FES(G)	FES2(S),PYRITE	FES2(S),MARCA	FE2MGO4(S)	FE203(S)
FE204SI(S)	FE204SI(L)	FE2012S3(S)	FE304(S)	H(G)	HMGO(G)	HNO(G)
HNO2(G),CIS-	HNO2(G),TRAS	HNO3(G)	HNA(S)	HNAO(S)	HNAO(L)	HNAO(G)
HO(G)	HO2(G)	H2(G)	H2MG(S)	H2MGO2(G)	H2NA202(G)	H20(G)
H202(G)	H204S(G)	H2S(G)	H3N(G)	MG(S)	MG(L)	MG(G)
MGO(S)	MGO(L)	MGO(G)	MGO3SI(S)	MGO3SI(L)	MGO4S(S)	MGO4S(L)
MGS(S)	MGS(G)	MG204SI(S)	MG204SI(L)	N(G)	NO(G)	NO2(G)
NO3(G)	N2(G)	N20(G)	N203(G)	N204(G)	N206(G)	NA(L)
NA(G)	NAO(G)	NA20(S)	NA20(L)	NA202(S)	NA203S(L)	NA203SI(S)
NA203SI(L)	NA204S(S),I	NA204S(S),DELTA	NA204S(L)	NA204S(G)	NA206SI2(S)	NA2S(S)
NA2S(L)	NA404SI(L)	NA607SI2(S)	O(G)	OS(G)	OSI(G)	O2(G)
O2S(G)	O2SI(S),QUARTZ,	O2SI(S),CRISTO-	O2SI(L)	O2SI(G)	O3(G)	O3S(G)
S(L)	S2(G)	S2SI(S)	S2SI(L)	SI(S)	SI(L)	SI(G)

The Following 66 Species are Being OMITTED. Preliminary Calculations Show That These Species Are Not Important For This System:

CCLH3(G)	CCLN(G)	CCL2(G)	CCL2H2(G)	CCL20(G)	CCL3(G)	CCL3H(G)	CH3CL3SI(G)
CS2(G)	CSI2(G)	C2HCL(G)	C2CL2(G)	C2CL4(G)	C2CL6(G)	C2H(G)	C2H40(G)
C2N(G)	C20(G)	C2SI(G)	C2N2(G)	C2N2NA2(G)	C302(G)	C4H12SI(G)	C4N2(G)
CA(G)	CLS(G)	HMG(G)	HN(G)	HNA(G)	HS(G)	HSI(G)	H2N(G)
H2N2(G)	H4N2(G)	H4SI(G)	N3(G)	MGN(G)	NS(G)	NSI(G)	NA2(G)
OS2(G)	S(G)	AL(L)	C(G)	ALC(G)	ALH(G)	ALN(G)	CSI(G)
C2(G)	C3(G)	C4(G)	C5(G)	CA2(G)	CL3SI(G)	CL4SI(G)	NSI2(G)
SSI(G)	S8(G)	SI2(G)	SI3(G)	NAO2(S)	FE03SI(S)	MG2SI(S)	MG2SI(L)
MG3N2(S)	N4SI3(S)						

The species selected in the solution phases are $Na_2O{\cdot}2SiO_2$, $MgO{\cdot}SiO_2$, NaCl, Na_2S, $FeO{\cdot}SiO_2$, and $CaO{\cdot}SiO_2$. The solution phases are chosen by performing trial calculations, with several possible combinations of components for the solution phases, based on a knowledge of solution chemistry and the thermodynamic tendency of components to form. Ideal solutions are assumed for the present calculations. Solution components are chosen in a manner that best illustrates the chemical properties and the simultaneously formed solutions that do not deviate significantly from the ideal. This procedure is a reasonable approximation for most of the cases where one cation (or anion) is the major component, and the concentrations of other cations and anions in the solution phase satisfy one of the following two conditions:

- Total concentration of other cations and/or anions is in the range of dilute solution, i.e., less than ≈10 mol%; and/or
- Any other cation(s) or anion(s) is (are) associated with the same anion(s) or cation(s) as the majority cation or anion, respectively.

In addition, the components are chosen in a manner that is consistent with the phase rule and the Gibbs–Duhem relation. Cases where solutions are not ideal, are not considered in these calculations.

COAL COMBUSTION

Coal combustion is usually carried out in the presence of excess oxygen or oxidant, where the SRO is greater than or equal to 1.0. First, we shall discuss a typical case where high–sulfur (3.41 wt.% S) Illinois coal is undergoing combustion with 30% excess oxygen, i.e., SRO = 1.3. We present the overall chemistry of condensed phases and the gaseous phase at SRO = 1.3. Second, we shall examine the effect of lower sulfur by assuming 1 wt.% S in the input coal. Finally, we shall vary the SRO from 1.0 to 1.3 and determine its effect on the overall chemistry of the combustion products. The resultant compositions are presented as a function of decreasing temperature to simulate the condition where the temperature of the combustion products is decreasing as they cool while passing through downstream components, away from the combustion zone.

Combustion of High–Sulfur Coal with 30% Excess Oxygen

Figures 6-9 describe the chemistry of combustion products from high-sulfur Illinois bituminous coal under oxidizing conditions when the SRO = 1.3. Of the 120 gaseous species considered, only the major species are shown in Figs. 6 and 7. Figures 8 and 9 present the variations in the chemistry of condensed phases,

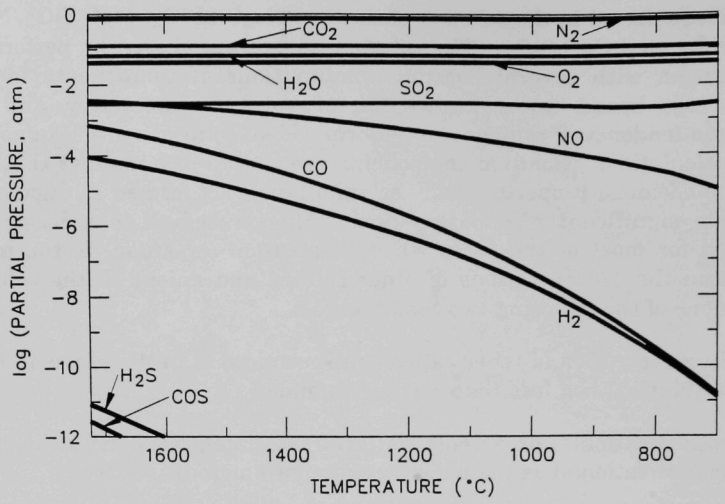

Fig. 6. Partial pressures of gaseous species during combustion of high-sulfur coal with 30% excess oxygen

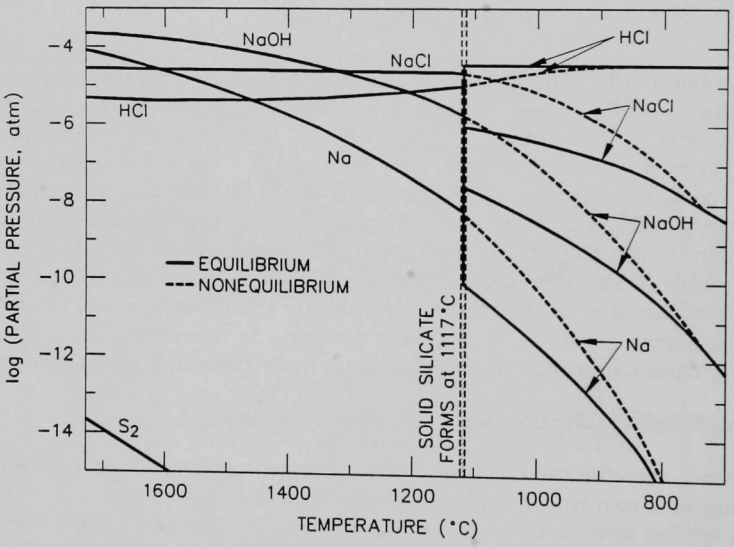

Fig. 7. Partial pressures of chlorine- and sodium-bearing gaseous species during combustion of high-sulfur coal

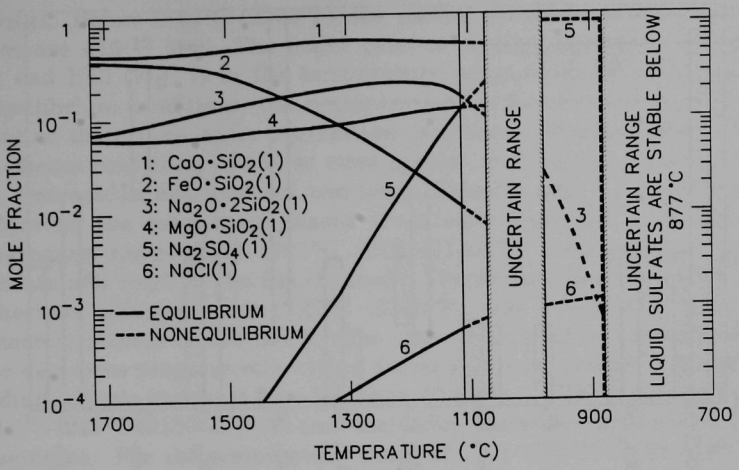

Fig. 8. Composition of liquid–solution phase for ideal mixing of designated species during the combustion of high–sulfur coal with 30% excess oxygen

including the solution phase. The variations in the composition of various solution phase components are summarized in Fig. 8. The approximate temperature ranges of stoichiometric condensed phases are shown in Fig. 9.

Equilibrium and Nonequilibrium Conditions

Under equilibrium conditions (see Fig. 7), abrupt changes in the partial pressures of several species such as NaCl(g), HC1(g), NaOH(g), and Na(g) occur near 1117°C (2040°F). Glassy $Na_2O \cdot Al_2O_3 \cdot 6SiO_2(s)$ is stable below ≈1117°C (2040°F) (indicated in Fig. 9). Furthermore, $Na_2SO_4(s)$ does not form (see Fig. 9) under equilibrium conditions at temperatures above 757°C, and a Na_2SO_4-rich liquid disappears (see Fig. 8) below 1117°C (2040°F). Formation of the $Na_2O \cdot Al_2O_3 \cdot 6SiO_2(s)$ phase is accompanied by disappearance of the silica-saturated liquid silicate-sulfate phase and by abrupt changes in the partial pressures of NaCl(g), HC1(g), NaOH(g), and Na(g).

Simultaneous changes in concentrations/partial pressures of several species can be analyzed with the following chemical reactions, which lead to the formation of a complex silicate:

$$3\ Al_2O_3 \cdot 2SiO_2(s) + 3\ Na_2O \cdot 2SiO_2(s \text{ or } 1) + 6\ SiO_2(s) = 3\ Na_2O \cdot Al_2O_3 \cdot 6SiO_2(s)$$

$$3\ Al_2O_3 \cdot 2SiO_2(s) + 12\ SiO_2(s) + 6\ NaCl(g) + 3\ H_2O(g) = 3\ Na_2O \cdot Al_2O_3 \cdot 6SiO_2(s) + 6\ HCl(g).$$

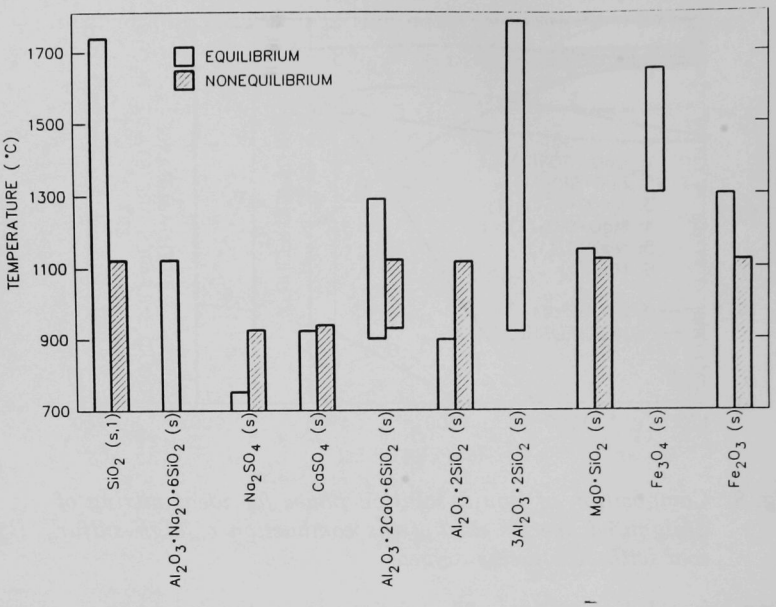

Fig. 9. Approximate temperature ranges for stability of condensed phases during combustion of high–sulfur coal with 30% excess oxygen

These chemical reactions are influenced by the supply of the reactants Al_2O_3, SiO_2, and NaCl. The influence of these reactants determines the amount of the product $Na_2O{\cdot}Al_2O_3{\cdot}6SiO_2(s)$. Because it forms by reactions between different and separated phases with imperfect contact, a nonequilibrium condition can result under which $Na_2O{\cdot}Al_2O_3{\cdot}6SiO_2(s)$ may not form. The calculations were repeated for such nonequilibrium conditions, and the results are presented in Figs. 7-9. Such a case simulates one kinetic constraint that can occur in a practical environment. Figure 9 shows that, under this constraint, the corrosive solution phase does not disappear at 1117°C (2040°F) but persists to temperatures as low as 887°C (1630°F). Use of such a nonequilibrium condition in the present calculations also demonstrates the capability of incorporating kinetic constraints in the analysis of the complex chemistry of coal combustion.

Gaseous- and Condensed-Phase Chemistry

Figure 6 shows that gaseous $N_2(g)$, $H_2O(g)$, $CO_2(g)$, and $O_2(g)$ constitute over 99 mol% of the total products. The partial pressure of $O_2(g)$ remains almost constant at the level of 0.04–0.05 atm. The major sulfur–bearing gaseous species

is SO_2(g). Below 1627°C (2960°F), the partial pressures of other sulfur–bearing species are $<10^{-12}$ atm. The major gaseous carriers of sodium and chlorine are NaCl and HCl (Fig. 7) in the temperature range of the present study. Under nonequilibrium conditions, the concentrations of NaCl(g) below 1117°C (2040°F) are higher than those under equilibrium conditions. Figures 8 and 9 indicate that solid phases consisting of one or more species, such as SiO_2, Al_2O_3, CaO, Na_2O, MgO, iron oxides, and sulfates, can form. Because there is an excess of silica in the system, the condensed phases are always saturated with silica. In the temperature range 1527-1727°C (2780-3140°F), calcium and iron silicates constitute >80 mol% of the liquid phase. The minor components are sodium and magnesium silicates. At 1727°C (3180°F), the concentration of sodium or magnesium silicate is <10 mol%. The concentration of iron silicate in the liquid phase decreases progressively with a decrease in temperature. The concentration of sodium silicate increases from less than 10 mol% at 1727°C (3180°F) to >20 mo % at ≈1177-1227°C (2150-2240°F) and, thereafter, decreases rapidly with a decrease in temperature. For the temperature range of 1127-1727°C (2060-3180°F), calcium silicate is the major component of the solution phase.

The concentration of Na_2SO_4 in the solution phase shows substantial variation as the temperature of the solution changes from 1727 to 727°C (3140 to 1340°F). Solubility of sulfate is <0.1 mol% above 1327°C (2420°F) but increases to almost 10 mol% at 1127°C (2060°F). At 1077°C (1970°F), under nonequilibrium conditions, Na_2SO_4 becomes the second major component of the solution phase (>20 mol%) and continues to increase rapidly with a decrease in temperature. Under nonequilibrium conditions, calcium silicate in the solution phase reacts to form a solid calcium aluminum silicate above 977°C (1790°F) or a sulfate at temperatures below 977°C (1790°F). Within the temperature range of 887-977 °C (1630-1790°F), the concentration of Na_2SO_4 in the solution phase is >90 mol%, and that of silicate is <10 mol%. At ≈887°C (1630°F), the silicate-sulfate solution phase that now contains >90 mol% Na_2SO_4 tends to disappear. However, if we consider a solution phase consisting of only sodium, magnesium, and calcium sulfates, the liquid phase would persist to somewhat lower temperatures. Treatment of such a ternary sulfate and a sulfate-silicate solution requires a detailed analysis of these complex mixtures.

The concentration values for various silicate species are expected to differ somewhat when a more accurate solution model is used. The concentrations indicated in our calculations are least accurate in the temperature range of 977-1077°C (1790-1970°F), because the expected deviations from the ideal solution model for the liquid silicate solutions with >10 mol% sulfate are large in this temperature range, which is designated as the uncertain region in Fig. 8. However, the agreement between the ideal and nonideal cases outside this uncertain region is reasonable, and the general pattern of most variations in the

concentration of silicates and sulfates as a function of temperature should be reasonably well represented by Fig. 8.

Based on the results of these calculations, the general behavior of the solution phase under oxidizing conditions can be described as follows. A liquid solution phase, consisting of mostly calcium, sodium, magnesium, and iron silicates, is represented at 1727°C (3140°F). The mole fraction of the Na_2SO_4 phase in the liquid is <0.01 at temperatures above 1277°C (2330°F). The concentration of Na_2SO_4 rises rapidly as the temperature decreases, and becomes a major component of the solution at 977°C (1790°F). The mole fraction of Na_2SO_4 may increase to 0.9 or more at 977°C (1790°F). These compositional changes can have implications for the corrosive behavior of the liquid condensates. The silicate liquid may be even more corrosive and have worse fouling tendencies than sulfates because of (a) high-temperature conditions, (b) adhesive behavior of the silicates, and (c) the solubility of ceramic components and protective oxide coatings of metals, which are probably higher in silicate than in sulfate melts.

Distribution of Chlorine, Sulfur, and Sodium

Figures 10-14 show the distribution of chlorine, sulfur, and sodium among the various phases of the combustion products. Results are presented in terms of mole percent of the input amount.

Chlorine. The major carriers of chlorine in combustion products are NaCl(l or g) and HCl(g) (see Fig. 10). At 1727°C (3140°F), NaCl(g) accounts for >81 mol% of the total chlorine input in the feedstock, and only 3.8 mol% of the input amount condenses as NaCl(l). The HCl(g) accounts for the rest of the 14.3 mol% of the input. At 1327°C (2420°F), a small amount of NaCl condenses. Within the temperature range of 1127-1327°C (2060-2420°F), the amount of chlorine present as HCl(g) and NaCl(l) increases to 26.4 and 11.4 mol%, respectively.

Under equilibrium conditions, NaCl in the solution phase disappears below ≈1027°C (1880°F), and HCl(g) becomes the major chlorine-bearing species (>99 mol% below 927°C or 1700°F). Under nonequilibrium conditions (not shown in Fig. 10), NaCl(l) phase continues to account for a significant fraction of the chlorine present (≈13.6 mol% at 927°C or 1700°F); the amount is similar to that of chlorine at equilibrium at 1127°C (2060°F). In any case, HCl(g) becomes the major carrier of chlorine (>50 mol%) at 1027°C (1880°F) under nonequilibrium conditions (see Fig. 10). Because the NaCl in the solution phase decreases to zero at 887°C (1630°F) under the nonequilibrium conditions, HCl(g) accounts for >91% of the input chlorine.

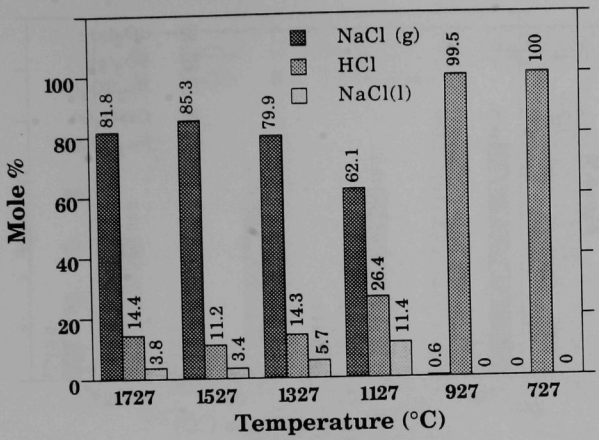

Fig. 10. Distribution of chlorine among different species at equilibrium during combustion of high-sulfur coal with 30% excess oxygen

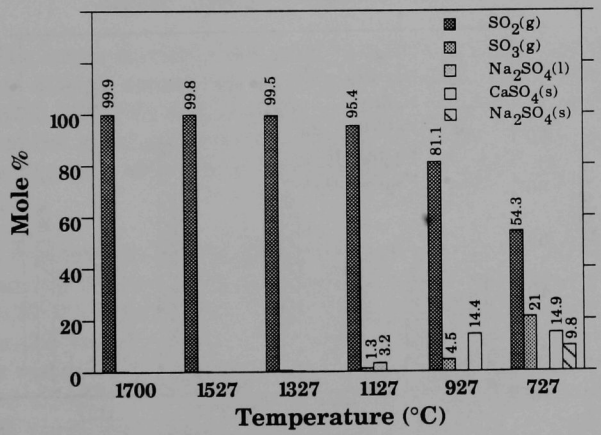

Fig. 11. Distribution of sulfur among different species at equilibrium during combustion of high-sulfur coal with 30% excess oxygen

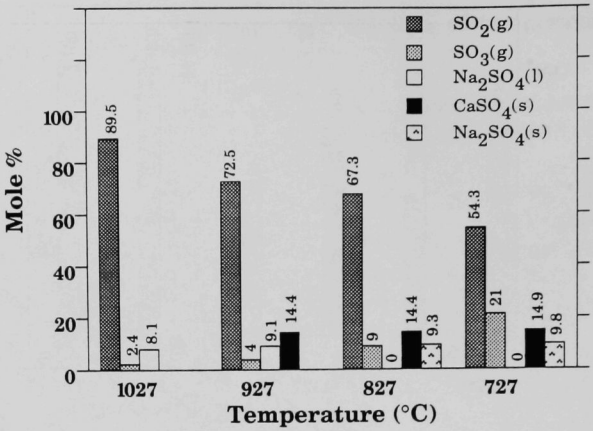

Fig. 12. Distribution of sulfur among different species under nonequilibrium conditions during combustion of high–sulfur coal with 30% excess oxygen

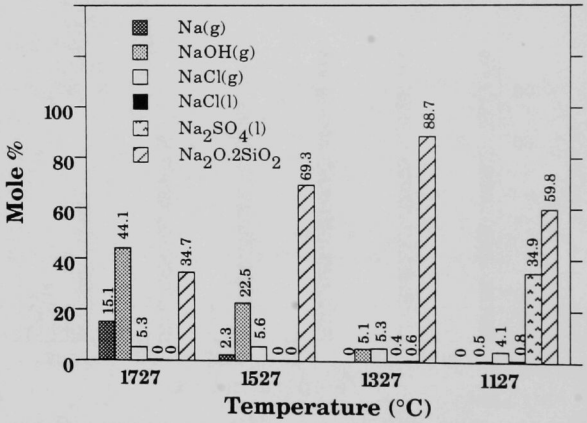

Fig. 13. Distribution of sodium among different species at equilibrium during combustion of high–sulfur coal with 30% excess oxygen

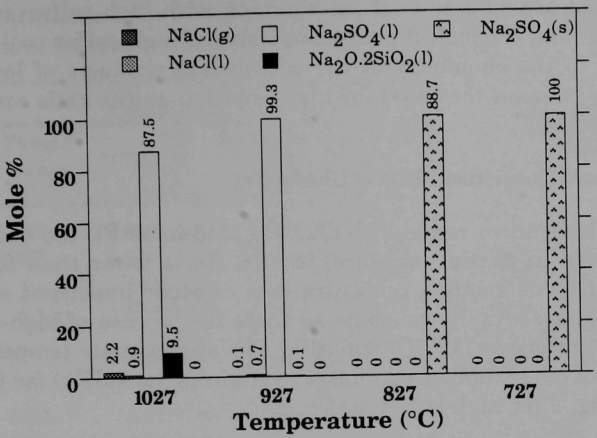

Fig. 14. Distribution of sodium between 1027 and 727°C for nonequilibrium conditions during combustion of high–sulfur coal with 30% excess oxygen

Sulfur. The major carrier of sulfur in the temperature range of 1127-1727°C (2060-3140°F) is SO_2(g), accounting for >99 mol% at 1327-1727°C (2420-3140°F), 95 mol% at 1127°C (2060°F), and 54 mol% at 727°C (1340°F). At 1127°C (2060°F), only 3.2 mol% of the input sulfur condenses as Na_2SO_4(l). Under nonequilibrium conditions (see Fig. 12), ≈9 mol% of the input sulfur is present as Na_2SO_4(l) at 927°C (1700°F).

Sodium. As shown in Fig. 13, the total amount of sodium as Na(g), NaOH(g), and NaCl(g) consists of ≈10.4, 30.4, and 64.5 mol% of the total input at 1327, 1527, and 1727°C (2420, 2780, and 3140°F), respectively. Most of the remaining sodium condenses into the liquid silicate. The content of sodium as Na_2SO_4(l) in the solution phase increases dramatically from 0.6 mol% at 1327°C (2420°F) to 34.9 mol% at 1127°C (2060°F). As the Na_2SO_4 content of the solution phase decreases below ≈1027°C (1880°F), almost all of the input Na is accounted for in the $Al_2O_3{\cdot}Na_2O{\cdot}6SiO_2$(s) compound at temperatures between 767°C (1410°F) and 1117°C (2040°F). Under nonequilibrium conditions, Na_2SO_4(l) contains >99.3% of the total Na at 927°C (1700°F). At temperatures below 827°C (1520°F), almost all of the sodium is present as Na_2SO_4(s).

Combustion of Low-Sulfur Coal with 30% Excess Oxygen

For the temperature range of 727-1727°C (1340-3140°F), the overall patterns in the behavior of gaseous- and condensed-phase chemistry during the combustion

of low-sulfur coal are similar to those obtained with high-sulfur coal. We shall use the gaseous- and condensed-phase chemistry of high-sulfur coal as a baseline for discussions of the chemistry of the combustion products of low-sulfur coal. The differences between the cases for high- and low-sulfur coals are described in the following sections.

Gaseous- and Condensed-Phase Chemistry

For the temperature range 727-1727°C (1340-3140°F), the concentration of $SO_2(g)$ (expressed in partial pressure) is ≈2.5 times lower than for the case of high-sulfur coal. The relative concentrations of other important sulfur-bearing species remained essentially the same as those in the case of high-sulfur coal at temperatures at or above 1127°C (2060°F). The approximate temperature ranges of the stability of other condensed phases (containing no sulfur) for both coals are identical (see Fig. 9 for high-sulfur coal).

The general trend in the variation of the solution–component concentrations for low-sulfur coal is the same as that for the high-sulfur coal (Fig. 8). Because of lower input amounts of sulfur in the case of low-sulfur coal, the concentration of the sulfur-bearing species, i.e., $Na_2SO_4(l)$, is lower. In Table 3, the concentrations of solution components are the same for the two coals at 1327-1727°C (2420-3140°F). For the temperature range 1427-1727°C (2600-3140°F), the concentrations of all the constituents are low for both cases. In the temperature range of 1027-1127°C (1880-2060°F), the amounts of $Na_2SO_4(l)$ are lower in the case of low–sulfur coal, being almost proportionally so at the lower concentrations. After adjusting for these differences in the concentrations of $Na_2SO_4(l)$, the concentrations of other solution components are similar for both coals. However, the probable formation of a multicomponent sulfate phase at lower temperature is not considered.

Distribution of Chlorine, Sulfur, and Sodium

Overall patterns of the relative distribution of chlorine, sulfur, and sodium among various phases for low-sulfur coal are also similar to those for high-sulfur coal. In the temperature range of 727-1727°C (1340-3140°F), the distribution of chlorine among various phases is not affected by the lower sulfur content in the coal. Major chlorine-bearing species are NaCl(g) and HCl(g). Lower amounts of sulfur in low-sulfur coal have an insignificant effect on the concentrations of NaCl(g) and HCl(g) in the combustion products.

At temperatures between 1227°C (2240°F) and 1727°C (3140°F), the concentration of $Na_2SO_4(l)$ in the combustion products is very low. Thus, the relative distribution of sodium and sulfur among various phases is not affected by the lower sulfur content of the coal. For the temperature range of 1117-1227°C

Table 3. Concentrations of solution–phase constituents for the combustion of high- and low-sulfur coals (SRO = 1.3)

	Equilibrium[a,b]			Nonequilibrium[a,b]		
	Temp.[c]	Mole Fraction		Temp.	Mole Fraction	
Liquid Components	Range (°C)	High–Sulfur	Low–Sulfur	Range (°C)	High–Sulfur	Low–Sulfur
$CaO{\cdot}SiO_2$	1627–	0.48–0.46	0.48–0.46	1077–	0.58–0.56	0.58–0.56
$Na_2O{\cdot}2SiO_2$	1727	0.08–0.10	0.08–0.10	1127	0.18–0.10	0.24–0.18
$MgO{\cdot}SiO_2$		0.06–0.06	0.06–0.06		0.12–0.12	0.12–0.13
$FeO{\cdot}SiO_2$		0.39–0.38	0.39–0.38		0.01–0.01	tr[b]
Na_2SO_4		<0.001	<0.001		0.10–0.21	0.05–0.13
NaCl		<0.001	<0.001		tr[d]	<0.001
$CaO{\cdot}SiO_2$	1327–	0.57–0.63	0.57–0.63	827–	–	–
$Na_2O{\cdot}2SiO_2$	1427	0.16–0.19	0.17–0.19	927	tr–0	0.01–0
$MgO{\cdot}SiO_2$		0.07–0.08	0.07–0.08		0.10–0	0.10–0
$FeO{\cdot}SiO_2$		0.19–0.10	0.19–0.10		tr–0	tr–0
Na_2SO_4		<0.001	<0.001		0.87–0	0.86–0
NaCl		<0.001	<0.001		0.02–0	0.03–0
$CaO{\cdot}SiO_2$	1027–	0.58–0	0.58–0			
$Na_2O{\cdot}2SiO_2$	1127	0.18–0	0.24–0			
$MgO{\cdot}SiO_2$		0.12–0	0.12–0			
$FeO{\cdot}SiO_2$		0.01–0	0.01–0			
Na_2SO_4		0.10–0	0.05–0			
NaCl		<0.001	<0.001			

[a]Under equilibrium and nonequilibrium conditions, solution phases are not stable below 1117 and 887°C, respectively.

[b]The concentrations correspond to temperatures as follows: for the temperatures of 1627 and 1727°C, the mole fractions of $CaO{\cdot}SiO_2$(l) are 0.46 and 0.48, respectively. Other solution components are read similarly.

[c]°F = °C x 1.8 + 32.

[d]tr = 0.001–0.01.

(2040-2240°F) under equilibrium conditions, and 927-1127°C (1700-2060°F) under nonequilibrium conditions, where a significant amount of sodium condenses as Na_2SO_4(l), the mole percent of sodium in the solution phase for the low-sulfur coal is appreciably lower than that of the high-sulfur coal.

For the temperature range of 727-1127°C (1340-2060°F), the distribution of sulfur for high- and low-sulfur coals is plotted in Figs. 15 and 16. Despite lower partial pressures of SO_2(g) in the gaseous phase (and the smaller amount of total sulfur) in the case of low-sulfur coal, the distribution of sulfur is similar for the high- and low-sulfur cases.

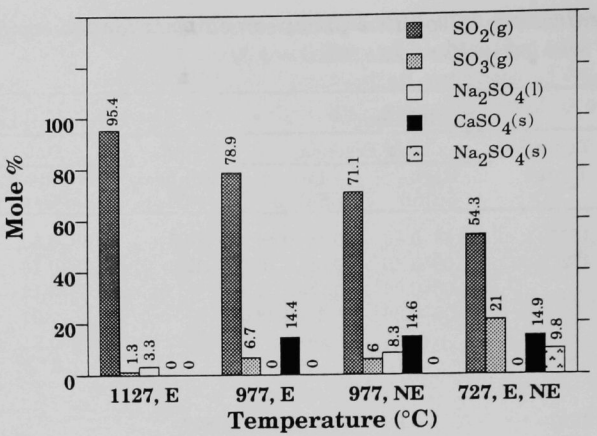

Fig. 15. Distribution of sulfur among different species between 1127 and 727°C at equilibrium (E) and nonequilibrium (NE) conditions during combustion of high-sulfur coal with 30% excess oxygen

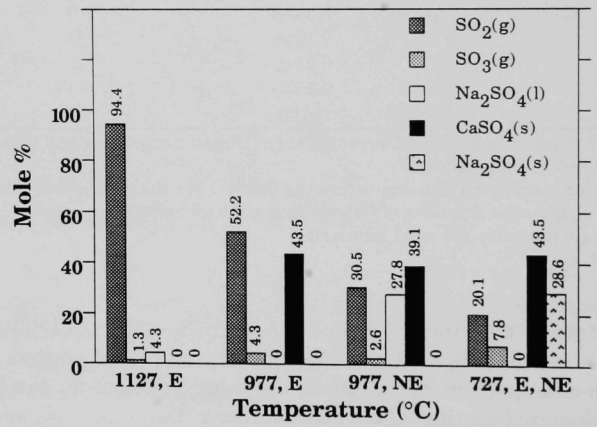

Fig. 16. Distribution of sulfur among different species between 1127 and 727°C at equilibrium (E) and nonequilibrium (NE) conditions during combustion of low-sulfur coal with 30% excess oxygen

Effect of Stoichiometric Ratio on the Chemistry of Combustion Products

In this section, we shall discuss the variations in the chemistry of combustion products as a function of the SRO in the range of 1.0-1.3. First we shall discuss the case for high-sulfur coal, then we shall deal with the effects of using lower–sulfur coal and discuss the differences between the two coals.

Combustion of High-Sulfur Coal

The variations in the concentrations of all the gas species as a function of decreasing temperature, at different values of SRO (1.02 to 1.3), are analogous to those reported for SRO = 1.3 (see Figs. 6 and 7). The absolute values of partial pressures of the gaseous species varied with changes in SRO. Figures 17-19 summarize the isothermal partial pressures of major gaseous species as continuous functions of SRO at temperatures of 727, 1127, and 1627°C (1340, 2060, and 2960°F).

For the SRO range of 1.02-1.30, the three curves representing the isothermal partial pressures of $H_2(g)$ at 727, 1127, and 1627°C (1340, 2060, and 2960°F) are almost parallel to each other (see Fig. 18). In Figs. 17-19, we can identify analogous behavior in partial pressures of $H_2S(g)$, $S_2(g)$, NaCl(g), HCl(g), NO(g), and $SO_2(g)$ (as functions of SRO and temperature). Moreover, for the SRO range of 1.05-1.30, the partial pressure of $O_2(g)$ is almost independent of temperature (in the range of 727-1627°C or 1340-2960°F). Partial pressures of key gaseous species, such as $H_2(g)$, $O_2(g)$, and $S_2(g)$, will largely dictate the overall chemistry of the combustion products. Because of close similarities in how the partial pressures of major gaseous species vary as a function of the SRO, the overall chemistry of combustion products is expected to be almost independent of SRO values in the range of 1.05-1.30. In addition, at any given value of the SRO >1.05, overall combustion-product chemistry will be the same as that when the SRO is 1.3. Figures 17-19 show that the absolute values of the partial pressures of various gas species may vary quite widely with temperature. However, the relative partial pressures of $O_2(g)$ and $SO_2(g)$ do not vary appreciably at different temperatures (Fig. 19).

Table 4, which summarizes the changes in the partial pressures of selected gaseous species as a function of temperature when the SRO = 1.05-1.30, shows that the partial pressure of HCl(g) increases with a decrease in temperature, but partial pressures of other gaseous species decrease with a decrease in temperature. If partial pressures of the gaseous species given in Table 4 are known at a given value of SRO, one may use the information in Table 4 to estimate the partial pressures of the same gaseous species for any other value of the SRO >1.05.

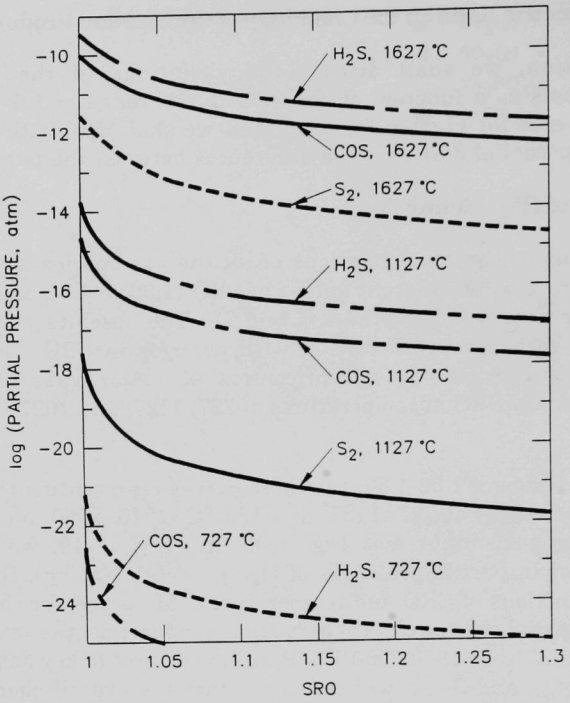

Fig. 17. Partial pressures of gaseous H_2S, COS, and S_2 in combustion products of high-sulfur coal as functions of SRO (air/fuel ratio)

The trend of the variation in the composition of solution phases as a function of a decrease in temperature at all levels of the SRO is similar to that when the SRO = 1.3 (Fig. 8). The changes in the concentrations of solution phases at three different levels of the SRO (1.01, 1.05, and 1.3) and at four temperature ranges are presented in Table 5. As can be seen in Table 5, some of the numerical values differ significantly with the SRO. Table 5 shows that at 1327°C (2420°F) and higher, the concentrations of the solution components do not vary greatly at different values of the SRO. Below 1127°C (2060°F), under both equilibrium and nonequilibrium conditions, the concentration of Na_2SO_4(l) is appreciably greater at higher values of the SRO. Approximate temperature ranges of the other condensed phases for all values of the SRO in the range of 1.0-1.3 are similar to those for the case when the SRO = 1.3 (see Fig. 9).

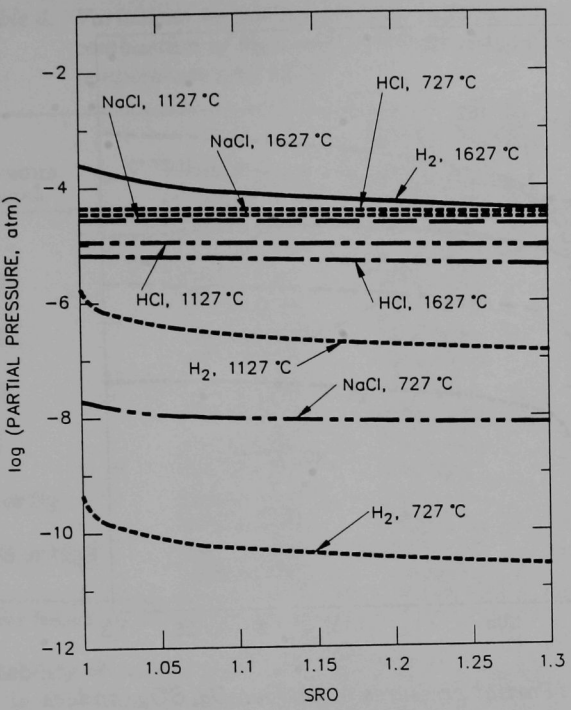

Fig. 18. Partial pressures of gaseous NaCl, HCl, and H_2 in combustion products of high-sulfur coal as functions of SRO (air/fuel ratio)

Combustion of Low-Sulfur Coal

Earlier discussions pertained to extensive similarities and certain small differences in the combustion–product chemistries of high- and low-sulfur coals at SRO of 1.3. Also, it was observed that, within the SRO range of 1.02-1.30, the combustion product chemistry does not vary greatly with SRO values. Thus, at any value of the SRO in the range of 1.05-1.3, the differences and similarities in the combustion product chemistry of low- and high-sulfur coals are expected to be very similar to those when the SRO = 1.3.

At any given value of the SRO and temperature, partial pressures of COS(g), H_2S(g), SO_2(g), and S_2(g) in the combustion products of low-sulfur coal are lower than those in the case of high-sulfur coal by factors of 10, 10^3-10^5, 10^3-10^5, and 10,

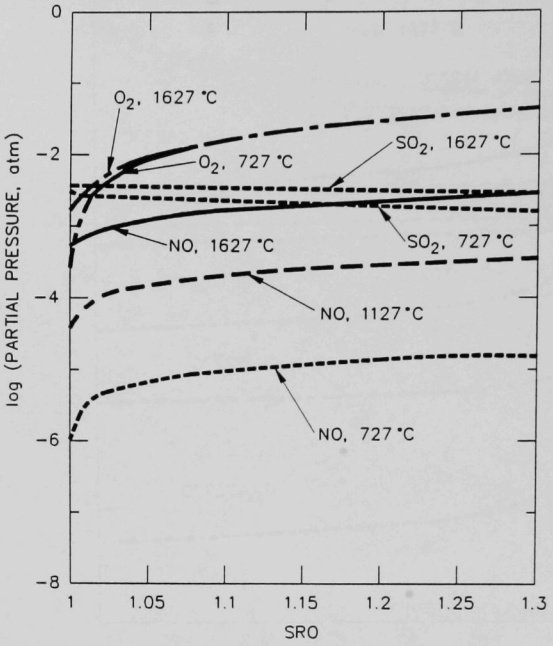

Fig. 19. Partial pressures of gaseous O_2, SO_2, and NO in combustion products of high–sulfur coal as functions of SRO (air/fuel ratio)

respectively. In addition, partial pressures of gaseous species with no sulfur, such as N_2(g), O_2(g), NO(g), HCl(g), NaCl(g), are approximately the same as those that occur in the case of high-sulfur coal (at all values of the SRO and temperatures used in our calculations).

Characteristics of the solution components during the combustion of low-sulfur coal are presented in Table 6 for three SRO values. In the temperature range of 1327-1727°C (2420-3140°F), the variation in the concentration of solution components is almost the same for high- and low-sulfur coals (compare Tables 5 and 6). In the temperature range of 727-1127°C (1340-2060°F), under both equilibrium and nonequilibrium assumptions, the concentration of the Na_2SO_4(l) is somewhat lower in the case of low-sulfur coal than that obtained in the case of high-sulfur coal. At any value of the SRO in the range of 1.05-1.3, the temperature

Table 4. Variations in partial pressures of gaseous species in combustion of high-sulfur coal as function of temperature and SRO

Gaseous Species	Temperature Decrease (°C)	Partial Pressure Change	
		Increase or Decrease	Factor[a]
O_2	1627 to 1127	–	1
	1400 to 1000	–	
SO_2	1900 to 1400	Decrease	≈1.03
	1400 to 1000	Decrease	≈1.06
NaCl	1900 to 1400	Decrease	≈1.3
	1400 to 1000	Decrease	≈3 x 10^3
HCl	1900 to 1400	Increase	2-4
	1400 to 1000	Increase	
NO	1900 to 1400	Decrease	8-10
	1400 to 1000	Decrease	
H_2 or S_2	1900 to 1400	Decrease	10^2–10^3
	1400 to 1000	Decrease	
COS or H_2S	1900 to 1400	Decrease	10^4–10^5
	1400 to 1000	Decrease	

[a]These factors are valid for any given SRO value in the range of 1.05–1.30.

range for stability of other condensed phases in the combustion products of low-sulfur coal is the same as that obtained with high-sulfur coal at SRO = 1.3 (see Fig. 9).

EXPERIMENTAL PROGRAM

The experimental program involves evaluation of candidate materials over the wide temperature range of 1000-1500°C (1832-2732°F) in environments that are relevant to HIPPSs. Some of the specific tasks are to study

(a) oxidation performance of materials in air environments,

(b) corrosion performance of materials in alkali salt environments,

(c) corrosion performance of materials in salt/slag environments,

(d) fracture toughness of materials as a function of temperature,

(e) influence of corrosion on the fracture toughness of materials,

(f) life prediction for heat recovery applications in HIPPS.

Table 5. Concentrations measured in mole fractions of solution components in high-sulfur coal under oxidizing conditions

Liquid Components	Equilibrium[a,b] Temp.[c] Range (°C)	SRO 1.01	SRO 1.05	SRO 1.30	Nonequilibrium[a,b] Temp. Range (°C)	SRO 1.01	SRO 1.05	SRO 1.30
$CaO{\cdot}SiO_2$	1627–	0.48–0.46	0.48–0.46	0.48–0.46	1027–	0.58–0.56	0.58–0.56	0.58–0.56
$Na_2O{\cdot}2SiO_2$	1727	0.08–0.10	0.08–0.10	0.08–0.10	1127	0.24–0.18	0.21–0.13	0.18–0.10
$MgO{\cdot}SiO_2$		0.06–0.06	0.06–0.06	0.06–0.06		0.11–0.12	0.12–0.12	0.12–0.12
$FeO{\cdot}SiO_2$		0.39–0.38	0.39–0.38	0.39–0.38		0.03–0.01	0.02–0.01	0.01–0.01
Na_2SO_4		<0.001	<0.001	<0.001		0.04–0.12	0.07–0.17	0.10–0.21
NaCl		<0.001	<0.001	<0.001		<0.001	<0.001	tr[d]
$CaO{\cdot}SiO_2$	1327–	0.49–0.59	0.53–0.61	0.57–0.63	827–	–	–	–
$Na_2O{\cdot}2SiO_2$	1427	0.14–0.18	0.15–0.18	0.16–0.19	927	0.01–0	tr–0	tr–0
$MgO{\cdot}SiO_2$		0.06–0.08	0.07–0.08	0.07–0.08		0.01–0	0.10–0	0.10–0
$FeO{\cdot}SiO_2$		0.31–0.16	0.25–0.12	0.19–0.10		tr–0	tr–0	tr–0
Na_2SO_4		<0.001	<0.001	<0.001		0.85–0	0.87–0	0.87–0
NaCl		<0.001	<0.001	<0.001		0.04–0	0.03–0	0.02–0
$CaO{\cdot}SiO_2$	1027–	0.58–0	0.58–0	0.58–0				
$Na_2O{\cdot}2SiO_2$	1127	0.24–0	0.21–0	0.18–0				
$MgO{\cdot}SiO_2$		0.11–0	0.12–0	0.12–0				
$FeO{\cdot}SiO_2$		0.03–0	0.02–0	0.01–0				
Na_2SO_4		0.04–0	0.07–0	0.10–0				
NaCl		<0.001	<0.001	<0.001				

[a]Under equilibrium and nonequilibrium conditions, solution phases are not stable below 1117 and 887°C, respectively.

[b]The concentrations correspond to temperatures as follows: for the temperatures of 1627 and 1727°C, the mole fractions of $CaO{\cdot}SiO_2$(l) are 0.46 and 0.48, respectively. Other solution components are read similarly.

[c]°F = °C x 1.8 + 32.

[d]tr = 0.001–0.01.

Materials

As a first step in selecting materials for the test program, a detailed literature survey was conducted to evaluate potential candidate materials with regard to composition, microstructure, fabrication process, mechanical and physical properties, chemical compatibility data, and track record of their applications at elevated temperatures. Based on this evaluation, we decided that

Table 6. Concentrations measured in mole fractions of solution components in low-sulfur coal under oxidizing conditions

	Equilibrium[a,b]				Nonequilibrium[a,b]			
	Temp.[c]	SRO			Temp.	SRO		
Liquid Components	Range (°C)	1.01	1.05	1.30	Range (°C)	1.01	1.05	1.30
$CaO{\cdot}SiO_2$	1627–	0.48–0.46	0.48–0.46	0.48–0.46	1077–	0.58–0.56	0.58–0.56	0.58–0.56
$Na_2O{\cdot}2SiO_2$	1727	0.08–0.10	0.08–0.10	0.08–0.10	1127	0.26–0.25	0.25–0.21	0.24–0.18
$MgO{\cdot}SiO_2$		0.06–0.06	0.06–0.06	0.06–0.06		0.11–0.12	0.12–0.12	0.12–0.13
$FeO{\cdot}SiO_2$		0.39–0.38	0.39–0.38	0.39–0.38		0.03–0.02	0.02–0.01	tr[d]
Na_2SO_4		<0.001	<0.001	<0.001		0.02–0.05	0.03–0.09	0.05–0.13
NaCl		<0.001	<0.001	<0.001		<0.001	<0.001	<0.001
$CaO{\cdot}SiO_2$	1327–	0.49–0.59	0.53–0.61	0.57–0.63	827–	–	–	–
$Na_2O{\cdot}2SiO_2$	1427	0.15–0.18	0.15–0.18	0.17–0.19	927	0.04–0	0.02–0	0.01–0
$MgO{\cdot}SiO_2$		0.06–0.08	0.07–0.08	0.07–0.08		0.10–0	0.10–0	0.10–0
$FeO{\cdot}SiO_2$		0.31–0.16	0.25–0.12	0.19–0.10		tr–0	tr–0	tr–0
Na_2SO_4		<0.001	<0.001	<0.001		0.81–0	0.84–0	0.86–0
NaCl		<0.001	<0.001	<0.001		0.05–0	0.04–0	0.03–0
$CaO{\cdot}SiO_2$	1027–	0.58–0	0.58–0	0.58–0				
$Na_2O{\cdot}2SiO_2$	1127	0.24–0	0.25–0	0.24–0				
$MgO{\cdot}SiO_2$		0.11–0	0.12–0	0.12–0				
$FeO{\cdot}SiO_2$		0.03–0	0.02–0	0.01–0				
Na_2SO_4		0.04–0	0.03–0	0.05–0				
NaCl		<0.001	<0.001	<0.001				

[a]Under equilibrium and nonequilibrium conditions, solution phases are not stable below 1117 and 887°C, respectively.

[b]The concentrations correspond to temperatures as follows: for the temperatures of 1627 and 1727°C, the mole fractions of $CaO{\cdot}SiO_2$(l) are 0.46 and 0.48, respectively. Other solution components are read similarly.

[c]°F = °C x 1.8 + 32.

[d]tr = 0.001–0.01.

the selected materials should exhibit good resistance to oxidation and corrosion in combustion atmospheres in the presence of salts (probably molten), high thermal conductivity, a low linear thermal expansion coefficient, good thermal shock resistance, and be available in product forms amenable to testing in a reasonable length of time. The materials selected for the experimental program include

advanced metallic alloys, monolithic ceramic materials, and ceramic–matrix ceramic composites; they are listed in Table 7, together with their manufacturers. As of this date, no metal–matrix ceramic composites have been selected.

Experimental Procedure

Coupon specimens, 2 cm x 2 cm x 1-2 mm, were prepared from several of the selected materials for air oxidation and salt exposure experiments. The dimensions and initial weights of the specimens were measured prior to exposure. The air oxidation tests were conducted in a resistant wound furnace at test temperatures of 1000, 1200, and 1400°C (1832, 2192, and 2552°F, respectively) for 168 h. In addition, preliminary tests were conducted with salt and salt/ash mixtures at 1000 (1832°F) and 1200°C (2192°F). Table 8 lists the preliminary tests that have been conducted thus far. Two salt mixtures were used in the experiments. In tests with Salt I, the specimens were immersed in the molten salt, which was contained in a boat. For tests with Salt II, the salt/ash mixture was finely ground and made into a water-based paste with which the specimens were coated at room temperature. The coated specimens were dried overnight and subsequently exposed to an air/SO_2 environment.

Results

The corrosion performance for some of the materials is described below.

Alumina

Monolithic alumina specimens were included in the test program to examine the salt effects on the corrosion degradation of the material. The flat plates of alumina were of high quality (96-98% alumina) and are generally used for substrate material in the electronic industry. In an air environment, alumina performed well at all temperatures. At 1400°C (2552°F), metallic alloy IN 671 melted, resulting in transfer of elements onto some of the ceramic materials exposed in the same boat; therefore, the test at 1400°C (2552°F) will be repeated at a later date.

During exposures to salt, the alumina specimens exhibited aluminum enrichment in the surface regions and presence of silicon, indicating some chemical reaction. The specimen exposed in Salt I at 1200°C changed color from bright white to bright blue and the specimen was brittle. The aluminum concentration in the surface of the specimen decreased substantially and enrichments in sodium and silicon were observed. In Salt II exposure at 1200°C (2192°F), aluminum enrichment and oxygen loss were observed. The same was true at 1000°C (1832°F) but to a lesser extent. The decrease in oxygen content in

Table 7. Materials selected for corrosion tests

Material	Manufacturer
Alumina	Coors Ceramics
Hexoloy SA	Carborundum
Hexoloy ST	Carborundum
SiC (I) particulate in alumina	Lanxide/DuPont
SiC (II) particulate in alumina	Lanxide/DuPont
Siliconized SiC (NT230)	Norton/TRW
Silicon nitride (NT154)	Norton/TRW
SiC in silicon matrix	INEX, Inc.
SiC fibers in SiC matrix	DuPont
SiC fibers in Si_3N_4 matrix	ORNL
5% Si_3N_4 (w) in Si_3N_4 matrix	ANL
CaO stabilized zirconia	Norton
Y_2O_3 stabilized zirconia	Norton
Inconel 671	INCO International
Inconel 617	INCO International

Table 8. List of oxidation/corrosion tests

Test Number	Test Environment[a]	Test Temperature (°C)
1	Air	1000
2	Air	1200
3	Air	1400
4	Salt I	1200
5	Salt II	1000
6	Salt II	1200

[a]Salt I composition: Na_2SO_4

Salt II composition: Na_2SO_4 (50%), SiO_2 (34%), and Al_2O_3 (16%)

Gas composition in salt tests: 1 vol.% SO_2 in air

salt-exposed specimens (when compared with air-exposed specimens) indicates that some ions high in oxygen and low in aluminum may have been dissolving in the salt. Table 9 gives the elemental analyses of specimens after several of the exposures.

Hexoloy SA

This material is a sintered form of alpha silicon carbide, with a density greater than 98% of theoretical. It has a very fine grain structure (8 μm) for excellent wear resistance and contains no free silicon, which has been reported to be chemically resistant in both oxidizing and reducing environments. In air tests, silicon carbide oxidized to form a silica layer, as evidenced by the oxygen content of the surface regions of the air-exposed specimens. At 1400°C (2552°F), all of the carbon in the surface region was oxidized to the gaseous form, which escaped with the flowing air. The resulting silicon was oxidized to silica, as evidenced by energy–dispersive X-ray (EDX) analysis.

In the Salt I exposure at 1200°C, the specimen melted, indicating formation of a low-melting (i.e., melting point <1200°C or 2192°F) compound by reaction of salt and silicon. Based on the Na_2O-SiO_2 phase diagram, additions of even a small amount of Na_2O to silica can lead to $Na_2O.x(SiO_2)$, with melting temperature decreasing with an increase in sodium oxide content. Because the pure Na_2SO_4 will establish fairly high Na_2O activity, especially at 1200°C (2192°F), the formation of the low-melting (Si,Na) compound is most likely.

In Salt II exposures at 1000 and 1200°C (1832 and 2192°F), the specimens exhibited somewhat less attack. The inner layers in these specimens were essentially silicon carbide, whereas the attack was confined to the surface regions. The influence of exposure time and temperature on surface reaction was examined from the elemental analyses for specimens exposed to Salt II at 1000 and 1200°C (1832 and 2192°F). The sodium oxide activity established by Salt II is probably much lower than that of Salt I. At 1000°C (1832°F), surface analysis indicates that silicon carbide reacts with oxygen to form silicon oxide, leading to enrichment of carbon at the surface in 168 h of exposure. At 1200°C (2192°F), the oxidation of silicon carbide to silicon oxide is virtually complete in 168 h of exposure. At longer exposure times, the reaction between silicon oxide and sodium oxide will occur and result in the low-melting (Si,Na) compound that was observed in Salt I exposure. Table 10 gives the elemental analyses of specimens after several of the exposures.

Table 9. Elemental analysis (wt.%) for alumina before and after testing

	As	Air		Air, 1000°C			Salt I, 1200°C			Salt II, 1000°C			Salt II, 1200°C		
Element	received	1400°C	1200°C	Surf.	Mid.	Inner	Surf.	Mid.	Inner	Surf.	Mid.	Inner	Surf.	Mid.	Inner
Al	52.9	43.6	48.1	60.1	70.0	60.8	14.8	75.0	78.6	34.9	83.2	74.0	92.7	75.3	85.1
O	47.1	45.3	43.0	37.9	27.9	25.2	38.6	23.4	20.0	1.6	14.5	25.1	0.9	9.9	12.7
Mg	–	6.7	8.2	–	–	12.4	–	–	–	–	–	–	–	–	–
Cr	–	4.4	–	–	–	–	–	–	–	–	–	–	–	–	–
Mo	–	–	0.6	1.5	2.1	1.7	–	–	–	–	–	–	–	3.8	–
Si	–	–	–	0.6	–	–	25.1	–	–	49.0	–	–	4.3	8.1	–
Na	–	–	–	–	–	–	18.0	0.9	0.4	9.5	1.2	0.4	1.0	3.0	0.9
Ca	–	–	–	–	–	–	0.7	–	–	–	–	–	–	–	–
S	–	–	–	–	–	–	2.8	0.8	1.0	5.1	1.0	0.5	1.2	–	1.3

Table 10. Elemental analysis (wt.%) for Hexoloy SA before and after testing

	As	Air		Air, 1000°C			Salt I, 1200°C			Salt II, 1000°C			Salt II, 1200°C		
Element	received	1400°C	1200°C	Surf.	Mid.	Inner	Surf.	Mid.	Inner	Surf.	Mid.	Inner	Surf.	Mid.	Inner
Si	48.0	46.7	29.2	99.9	61.3	47.3	M[a]	M	M	26.1	74.9	46.1	65.9	33.6	44.2
C	52.0	–	56.8	–	38.7	52.5	M	M	M	72.7	24.2	53.8	–	64.9	55.1
O	–	53.3	14.1	0.1	–	0.2	M	M	M	0.9	0.5	–	30.6	0.6	0.2
Na	–	–	–	–	–	–	M	M	M	0.1	0.1	–	1.0	0.8	0.1
Al	–	–	–	–	–	–	M	M	M	0.2	0.1	0.1	1.4	0.1	0.1
Ti	–	–	–	–	–	–	M	M	M	–	–	–	1.2	–	0.2
S	–	–	–	–	–	–	M	M	M	–	0.3	–	–	–	–

[a]Specimen contaminated by melted alloys 671 and 617.

SiC in Silicon Matrix

This material, developed by INEX, Inc. under the sponsorship of Gas Research Institute, consists of SiC grains surrounded by a silicon matrix and is reported to have zero porosity. Tubes of this material have been tested at elevated temperatures in oxidizing environments, but not in combustion atmospheres. In air tests, the silicon carbide was oxidized to form a silica layer, as evidenced by the oxygen content of the surface regions of the air-exposed specimens. In air oxidation, the behavior of this material is similar to that of Hexoloy SA at all temperatures. The surface of the oxidized samples showed deep pores and big cracks. At 1400°C (2552°F) in air, the silicon carbide was converted to silica and this conversion occurred to a lesser extent at lower temperatures. Additional testing is needed to establish the temperatures and oxygen partial pressures that are critical for the "active" versus "passive" oxidation of silicon produced by reduction of silicon carbide.

In Salt I exposure at 1200°C (2192°F), the specimen melted because the low-melting (Si,Na) phase discussed before had formed. In Salt II exposure, the oxidation or conversion of silicon carbide into silicon oxide occurred. At 1200°C (2192°F), the carbide was completely converted into oxide; the performance of this

material is similar to that of Hexoloy SA. Table 11 shows the elemental analyses of specimens after several of the exposures.

SiC Fiber/SiC Matrix

This material is made by DuPont by a chemical vapor infiltration process. The material, recommended for service that requires high strength, high-temperature properties, and light weight, was air tested only at 1000°C (1832°F) because it was procured after completion of the 1200 and 1400°C (2192 and 2552°F) tests. At 1000°C (1832°F) in air, the specimen exhibited some oxygen pickup and silicon loss but these were confined to the surface region.

In Salt I exposure at 1200°C (2192°F), the specimen melted and behaved in a manner similar to other SiC specimens that were discussed earlier. In Salt II exposures, the EDX analysis shows that silicon concentration at the surface of the specimen at 1000°C (1832°F) is essentially the same as that in the inner layer of the specimen exposed at 1200°C (2192°F). At present, it is not clear whether the 1200°C (2192°F) morphology will occur in the 1000°C (1832°F) sample after longer exposure time. Additional testing is needed to clarify the role of salt constituents in the corrosion process. Table 12 gives the elemental analyses of specimens after several of the exposures.

Si_3N_4 Whiskers in Si_3N_4 Matrix

This material was developed at ANL and consists of 5 vol.% Si_3N_4 whiskers in a Si_3N_4 matrix. The material has shown superior fracture toughness and other mechanical properties at elevated temperatures. Air oxidation of the material shows substantial reduction in nitrogen content. In addition, significant migration of Mg from the interior of the material to the surface was observed. The Mg migration was small at 1000°C (1832°F), but increased to 26.5 and 27.2 wt.% at 1200 and 1400°C (2192 and 2552°F), respectively. Furthermore, the sample exposed at 1400°C lost all of its nitrogen in 168 h.

The material was not tested in the Salt I environment because a sufficient amount of material was not available to conduct all the tests. In Salt II exposure at 1000°C (1832°F), the material exhibited salt constituents on the sample surface but the interior of the specimens maintained the silicon nitride composition. At 1200°C (2192°F) in Salt II, the sample surface showed some decrease in nitrogen concentration and an increase in oxygen concentration, indicating oxidation of silicon nitride, but the salt constituents did not seem to have any significant effect. Additional testing is needed to substantiate this result and to establish the performance envelope for the material in terms of salt chemistry, temperature, and exposure time. Table 13 gives the elemental analyses of specimens after several of the exposures.

Table 11. Elemental analysis (wt.%) for SiC / Si before and after testing

	As	Air		Air, 1000°C			Salt I, 1200°C			Salt II, 1000°C			Salt II, 1200°C		
Element	received	1400°C	1200°C	Surf.	Mid.	Inner	Surf.	Mid.	Inner	Surf.	Mid.	Inner	Surf.	Mid.	Inner
Si	51.1	46.7	27.0	45.0	–	–	M[a]	M	M	10.4	44.9	94.1	65.0	31.0	–
C	48.5	–	60.2	54.8	–	–	M	M	M	–	54.2	–	–	38.0	–
O	0.4	53.3	11.1	0.2	–	–	M	M	M	15.1	0.2	2.1	15.1	17.9	–
Mo	–	–	1.8	–	–	–	M	M	M	–	11.5	–	–	–	–
Al	–	–	–	–	–	–	M	M	M	–	–	–	12.7	6.8	–
Na	–	–	–	–	–	–	M	M	M	28.4	0.3	1.8	7.3	6.3	–
K	–	–	–	–	–	–	M	M	M	0.7	–	0.2	–	–	–
S	–	–	–	–	–	–	M	M	M	33.9	0.3	1.9	–	–	–

[a]Specimen contaminated by melted alloys 671 and 617.

Table 12. Elemental analysis (wt.%) for SiC / SiC before and after testing

	As	Air		Air, 1000°C			Salt I, 1200°C			Salt II, 1000°C			Salt II, 1200°C		
Element	received	1400°C	1200°C	Surf.	Mid.	Inner	Surf.	Mid.	Inner	Surf.	Mid.	Inner	Surf.	Mid.	Inner
Si	70.0	NA[a]	NA	53.8	48.4	66.6	M[b]	M	M	94.2	46.3	73.3	3.5	60.0	93.9
C	30.0	NA	NA	44.4	51.4	33.2	M	M	M	–	53.5	–	59.2	38.0	–
O	–	NA	NA	1.8	0.2	0.2	M	M	M	4.9	–	4.2	17.0	1.9	4.0
Al	–	NA	NA	–	–	–	M	M	M	–	–	–	0.6	0.1	0.8
Na	–	NA	NA	–	–	–	M	M	M	0.6	–	11.9	12.1	0.2	0.6
K	–	NA	NA	–	–	–	M	M	M	–	–	–	0.5	–	–
Cl	–	NA	NA	–	–	–	M	M	M	–	–	–	3.9	–	0.3
S	–	NA	NA	–	–	–	M	M	M	0.2	0.2	10.6	3.2	–	0.4

[a]Not available. [b]Specimen contaminated by melted alloys 671 and 617.

Table 13. Elemental analysis (wt.%) for Si_3N_4 (W) / Si_3N_4 before and after testing

	As	Air		Air, 1000°C			Salt I, 1200°C			Salt II, 1000°C			Salt II, 1200°C		
Element	received	1400°C	1200°C	Surf.	Mid.	Inner	Surf.	Mid.	Inner	Surf.	Mid.	Inner	Surf.	Mid.	Inner
Si	59.2	42.8	31.4	57.0	57.7	56.8	NA[a]	NA	NA	2.3	56.0	57.7	42.9	58.2	58.6
N	39.4	-	20.9	37.9	38.4	37.8	NA	NA	NA	1.5	37.2	38.3	28.5	38.7	39.0
Mg	1.4	27.2	26.5	0.8	0.3	2.3	NA	NA	NA	–	5.4	1.4	–	2.2	1.3
O	–	21.8	20.4	3.4	1.2	0.8	NA	NA	NA	15.7	1.4	–	26.7	–	–
Ca	–	5.0	0.9	–	–	–	NA	NA	NA	–	–	–	–	–	–
Al	–	3.1	–	–	–	–	NA	NA	NA	–	–	0.5	0.6	0.3	0.4
Mo	–	–	–	0.9	2.5	2.4	NA	NA	NA	12.1	–	1.4	–	0.4	0.7
Na	–	–	–	–	–	–	NA	NA	NA	43.5	–	0.8	1.4	0.3	–
S	–	–	–	–	–	–	NA	NA	NA	24.9	–	–	1.4	0.3	–

[a]Not available

CaO-Stabilized Zirconia

This material, included in the program because of its superior high-temperature mechanical properties, was tested under all exposure conditions and performed well. The specimen exposed to air at 1400°C (2552°F) showed a surface deposit of Mo, probably vaporized from the upstream sample of Inconel 617, which

contained 11.8 wt.% Mo. Similar deposition of Cr in the 1200°C (2192°F) sample was noted. These tests must be repeated and will be conducted when we test other ceramic/composite materials, which are yet to be received from various vendors. The specimen exposed to air at 1000°C (1832°F) shows some migration of calcium and silicon from the interior of the specimen to the surface region. The calcium content at the surface was 11.5 wt.% after 168 h exposure at 1000°C (1832°F).

In the Salt I exposure at 1200°C (2192°F), the specimen was covered with the melt that formed from other specimens. In Salt II exposures, the specimens performed well. The specimens exhibited loss of calcium and oxygen from the surface regions at 1000 and 1200°C (1832 and 2192°F) and surface enrichment of zirconium. Loss of calcium may lead to changes in crystal structure of the material that can affect mechanical properties. Additional tests are planned to evaluate the role of corrosion on the mechanical properties of these materials. Table 14 gives the elemental analyses of specimens after several of the exposures.

Table 14. Elemental analysis (wt.%) for CaO/ZrO_2 before and after testing

	As	Air		Air, 1000°C			Salt I, 1200°C			Salt II, 1000°C			Salt II, 1200°C		
Element	received	1400°C	1200°C	Surf.	Mid.	Inner	Surf.	Mid.	Inner	Surf.	Mid.	Inner	Surf.	Mid.	Inner
Zr	71.3	3.5	77.7	54.7	69.0	62.1	2.2	64.5	94.4	92.9	92.6	91.4	95.3	91.8	32.8
O	25.0	7.9	7.5	23.8	25.1	22.9	25.3	10.5	1.4	2.9	4.4	3.1	2.8	3.9	4.9
Ca	2.3	24.4	9.5	11.5	2.4	2.8	0.5	0.6	2.5	2.7	0.3	2.8	–	0.6	2.7
Si	2.0	–	–	10.0	2.1	4.8	16.9	6.2	0.4	–	–	0.2	0.3	0.2	0.5
Al	–	–	–	–	1.4	7.5	8.5	5.8	–	–	–	–	–	–	–
Mo	–	64.2	–	–	–	–	–	–	–	–	–	–	–	–	–
Cr	–	–	5.3	–	–	–	–	–	–	–	–	–	–	–	–
Na	–	–	–	–	–	–	31.1	9.0	0.2	–	0.7	0.4	0.4	1.8	29.7
S	–	–	–	–	–	–	15.3	3.5	1.2	1.6	2.0	2.1	1.2	1.8	11.5

SUMMARY

A computer program that is based on geometric programming and can be applied to a chemical system containing a large number of species was used to calculate the chemistry of the products of coal conversion. Concentrations of all the gaseous and condensed species were determined for a coal with two sulfur levels, temperatures, and air/fuel ratios. Of the 120 gaseous species considered, partial pressures of N_2, CO_2, H_2O, O_2, SO_3, HCl, NO, NaCl, Na_2SO_4, NaOH, H_2, H_2S, and S_2 were used to represent the chemistry of the coal-conversion products. Conclusions reached from these calculations are presented below.

Coal combustion forms a liquid phase that is essentially a silica-saturated silicate-sulfate condensate, with the components being largely $CaO{\cdot}SiO_2$, $Na_2O{\cdot}2SiO_2$, $FeO{\cdot}SiO_2$, $MgO{\cdot}SiO_2$, Na_2SO_4, and NaCl. Compounds containing

alumina, which may be present at concentrations <10 mol%, were not considered in the analysis. At temperatures below 1177°C (2150°F), partial pressures of NaCl(g), HCl(g), NaOH(g), and Na(g) change abruptly, a complex sodium aluminosilicate, $Na_2{\cdot}Al_2O_3{\cdot}6SiO_2(s)$, tends to form, and the liquid silicate-sulfate condensate disappears. Formation of the complex silicate requires intimate contact among several gaseous and condensed phases, the probability of which is expected to be low in practical systems. Furthermore, experimental and industrial observations provide evidence of stable sulfate-rich condensates under similar conditions.[6] It is, therefore, probable that the chemical reactions leading to the formation of the complex silicate do not go to completion in coal-conversion systems. Under nonequilibrium conditions, where such reactions are constrained, the stability of the sulfate–silicate condensate extends to temperatures as low as 887°C (1630°F).

The $N_2(g)$, $H_2O(g)$, $CO_2(g)$, $O_2(g)$ species constitute over 99 mol% of the total effluent in coal combustion. The partial pressure of $O_2(g)$ remains almost independent of temperature at 0.04 to 0.06 atm. The major sulfur-bearing species is SO_2, which has partial pressures of 0.002-0.004 atm and 0.001-0.002 atm for high- and low-sulfur coals, respectively. At high temperatures, NaOH(g) is the major sodium-containing species; below 1377°C (2510°F), NaCl(g) predominates. At temperatures above 1127°C (2060°F), the partial pressures of NaOH(g) and/or NaCl(g) are of the order of 10^{-4} atm. Within the temperature range of 1127-1727°C (2060-3140°F), HCl(g) and NaCl(g) are the major chlorine-bearing species, the partial pressure of which varies within the relatively close range of 5×10^{-4} to 2×10^{-5} atm. Below 1127°C (2060°F), the partial pressure of NaCl(g) decreases with a decrease in temperature; however, partial pressures of HCl continue to stay at $\approx 10^{-4}$ atm. Partial pressures of $O_2(g)$, $CO_2(g)$, $H_2(g)$, NaCl(g), NaOH(g), and HCl(g) appear to be independent of the amount of sulfur in the input coal.

Above 1327°C (2420°F), the solution consists of mostly $CaO{\cdot}SiO_2$, $Na_2O{\cdot}SiO_2$, and $FeO{\cdot}SiO_2$ as well as traces of Na_2SO_4. As the temperature decreases, the concentration of $FeO{\cdot}SiO_2$ decreases and that of Na_2SO_4 increases. At 1127°C (2060°F), the concentration of Na_2SO_4 may be relatively high (≈12 mol% for high-sulfur coal) and may increase very rapidly with a decrease in temperature. Under nonequilibrium conditions, the solution phase is rich in Na_2SO_4. For high-sulfur coal at temperatures below 927°C (1700°F), the solution phase consists of >90 mol% sulfate. A solution phase consisting of sodium, magnesium, and calcium sulfates is stable below 877°C (1612°F). The transition from silicate sulfate to sulfates occurs within the temperature range of 977-1127°C (1790-2060°F). Apart from the silica-saturated silicate-sulfate solution phase, other (one or more) solid phases containing the following compounds are possible: Al_2O_3, CaO, MgO, iron oxides, and SiO_2 (SiO_2 can also form a separate liquid at high temperatures). The behavior of silicate-sulfate liquids as a function of

temperature is not affected by differing sulfur contents in coal. For low-sulfur coal, the amount of $Na_2SO_4(l)$ is, however, slightly lower at temperatures below 1127°C (2060°F), where it is present in significant amounts.

Calculations on the distribution of chlorine, sulfur, and sodium in various phases showed that below 927°C (1700°F), the main depository of chlorine is HCl(g). At temperatures above 1127°C (2060°F), $SO_2(g)$ and $SO_3(g)$ account for >95% of the sulfur input. At temperatures below 927°C (1700°F), >14 mol% of sulfur input condenses in some form. Sodium usually condenses as silicates and/or sulfates. For the SRO range of 1.02 to 1.30, the trend in the variation in partial pressures of major gaseous species [$H_2(g)$, $O_2(g)$, $S_2(g)$, $H_2S(g)$, NaCl(g), NO(g), and $SO_2(g)$] as a function of the SRO and of temperature is similar. The absolute values of partial pressures of all the gaseous species except $O_2(g)$ and $SO_2(g)$ vary widely for various values of the SRO. At any value of the SRO in the range of 1.0-1.3, the correlation between concentrations of solution components and temperature is very similar to that at SRO = 1.3. At temperatures ≥1327°C (2420°F) and higher values of the SRO, concentrations of $Na_2O{\cdot}2SiO_2(l)$ tend to be higher, whereas those of $FeO{\cdot}SiO_2(l)$ tend to be lower. For the SRO range of 1.05-1.30, the differences and similarities in combustion-product chemistry of low- and high-sulfur coals are analogous to those at a SRO of 1.3. Partial pressures of COS(g), $H_2S(g)$, $SO_2(g)$, and $S_2(g)$ were lower in the case of low-sulfur coal. At higher temperatures (1427-1727°C or 2600-3180°F), concentrations of $Na_2SO_4(l)$ were not affected by the sulfur content of the coal. Below 1427°C (2600°F), the concentration of $Na_2SO_4(l)$ was lower in the case of low-sulfur coal.

An experimental program has been initiated to evaluate materials for advanced combustion systems. Several candidate materials have been identified for evaluation. The materials included advanced metallic alloys, monolithic ceramics, ceramic particulate/ceramic matrix composites, ceramic fiber/ceramic matrix composites, and ceramic whisker/ceramic matrix composites. The candidates are nickel-based superalloys, alumina, stabilized zirconia, various types of silicon carbide, and silicon nitride. Coupon specimens of several of the materials have been tested in an air environment at 1000, 1200, and 1400°C (1832, 2192, and 2552°F) for 168 h. In addition, specimens were exposed to sodium sulfate containing salts at temperatures of 1000 and 1200°C (1832 and 2192°F) for 168 h. Extensive microstructural analysis was conducted on exposed specimens to evaluate the corrosion performance of the materials for service in air and fireside environments of advanced coal-fired boilers. Additional tests are in progress with several of the materials to evaluate the corrosion performance of these materials as function of salt chemistry, salt deposition rate, alkali vapor concentration, gas chemistry, exposure temperature, and exposure time.

ACKNOWLEDGMENTS

The authors acknowledge several manufacturers of ceramic materials for the supply of specimen materials. Yanez-Herrero and Fornasieri were supported by financial assistance under a student exchange program. D. L. Rink assisted in the corrosion tests and microstructural analysis of the exposed specimens.

REFERENCES

1. Annual Energy Review 1990, DOE/EIA-0834, Energy Information Administration, U.S. Department of Energy.
2. L. A. Ruth, "Combustion 2000," PETC Review, Issue 4, p. 4, Fall 1991.
3. J. Shenker, "Development of a High-Performance Coal-Fired Power-Generating System with a Pyrolysis Gas and Char-Fired High-Temperature Furnace," Proc. Ninth Annual Coal Preparation, Utilization, and Environmental Control Contractors Conference, U.S. DOE, Pittsburgh Energy Technology Center, Pittsburgh, PA, 1993, p. 349.
4. D. J. Seery, J. J. Sangiovanni, F. L. Robson, W. M. Proscia, J. E. Holowczak, M. Bak, J. D. Freihaut, M. Heap, D. W. Pershing, and P. J. Smith, "Combustion 2000: Burning Coal in the Twenty-First Century," ibid., p. 356.
5. R. K. Ahluwalia, K. H. Im, K. Natesan, C. D. Livengood, and D. K. Schmalzer, "Technical Support for Combustion 2000 Program," ibid., p. 226.
6. S. N. Sinha, K. Natesan, and M. Blander, "Chemistry of Gaseous and Condensed Products in Coal Combustion and Conversion Systems," Argonne National Laboratory Report ANL-89/25 (1989).
7. M. Minkoff, R. Land, and M. Blander, "Computation of Chemical Equilibria via Primal Geometric Programming," CALPHAD XI Conf., Argonne National Laboratory, Chicago, May 16–20, (1982).
8. R. J. Duffin, E. L. Peterson, and C. Zener, Geometric Programming – Theory and Applications, John Wiley and Sons, New York, pp. 255–264 (1965).
9. R. Kumar, M. L. Saboungi, and M. Blander, Argonne National Laboratory, unpublished (1981).
10. M. W. Chase, Jr., C. A. Davies, J. R. Downey, Jr., D. J. Frurip, R. A. McDonald, and A. N. Syverud, "JANAF Thermochemical Tables," J. Phys. Chem. Ref. Data, 14, Supplement No. 1 and 2, and earlier supplements (1985).
11. I. Barin, O. Kancke, and O. Kubaschewski, "Thermochemical Properties of Inorganic Substances," 1973 and 1975 Supplements, Springer–Verlag, Berlin.

12. R. A. Rokie, B. S. Hemingway, and J. R. Fisher, "Thermodynamic Properties of Minerals and Related Substances at 298.15 K and 1 Bar (10^5 Pascals) Pressure and at Higher Temperatures," U.S. Geological Survey Bulletin No. 1452 (1984).

13. L. B. Pankratz, J. M. Stuve, and N. A. Gokcen, "Thermodynamic Data for Mineral Technology," U.S. Bureau of Mines Bulletin No. 677 (1984).

14. B. J. McBride and S. Gordon, FORTRAN IV Program for Calculations of Thermodynamic Data, National Aeronautics and Space Administration Report, TN, D–4097 (1967).

15. S. Gordon and B. J. McBride, Computer Program for Calculations of Complex Chemical Equilibrium Compositions, National Aeronautics and Space Adminstration Report, N78–17724 (1971).

Appendix A:

Macrophotographs of Specimens before and after Testing

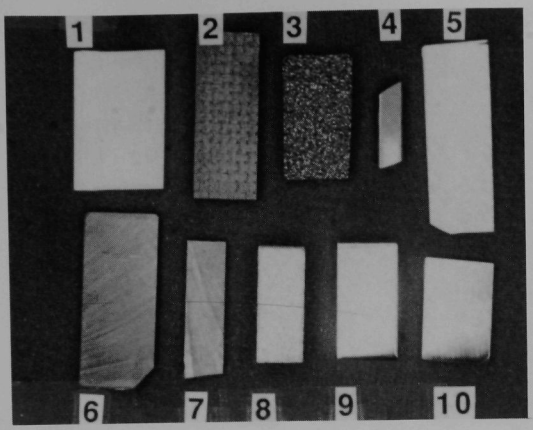

1. Alumina
2. SiC/SiC
3. SiC/Si
4. $Si_3N_4(w)/Si_3N_4$
5. ZrO_2 (Y_2O_3)
6. Hexoloy SA
7. Hexoloy ST
8. ZrO_2 (CaO)
9. Inconel 671
10. Inconel 617

Fig. A–1. Specimens before oxidation/corrosion testing

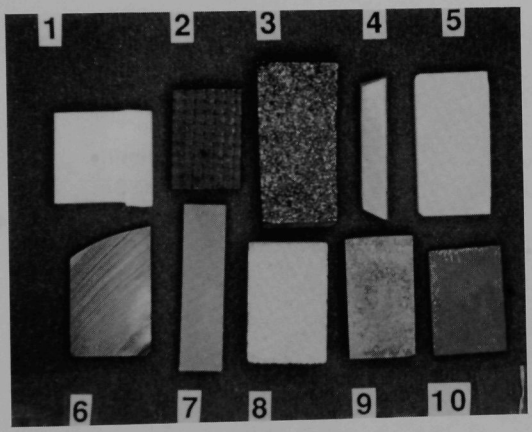

1. Alumina
2. SiC/SiC
3. SiC/Si
4. $Si_3N_4(w)/Si_3N_4$
5. ZrO_2 (Y_2O_3)
6. Hexoloy SA
7. Hexoloy ST
8. ZrO_2 (CaO)
9. Inconel 671
10. Inconel 617

Fig. A–2. Specimens after 168–h exposure in air at 1000°C

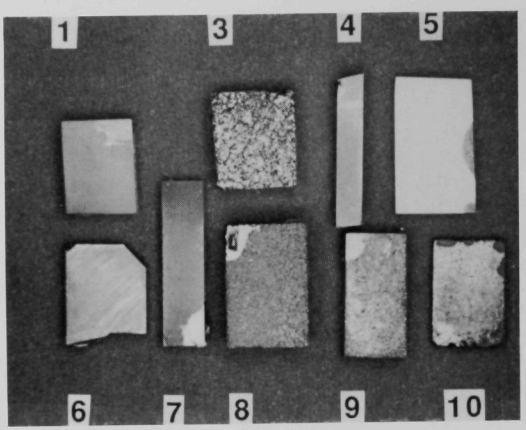

Fig. A–3. Specimens after 168–h exposure in air at 1200°C

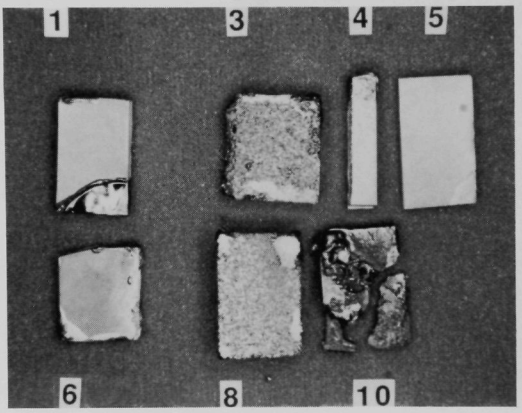

Fig. A–4. Specimens after 168–h exposure in air at 1400°C

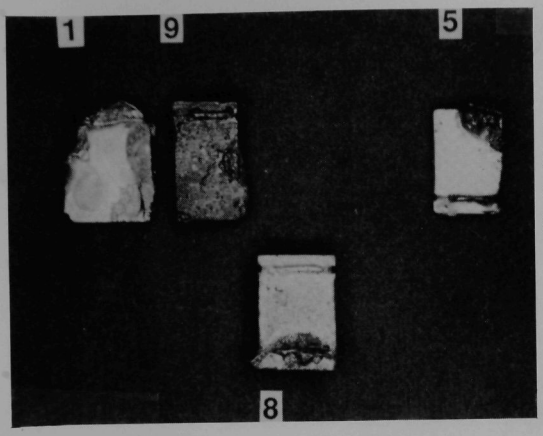

Fig. A–5. Specimens after 168–h exposure in salt I at 1200°C

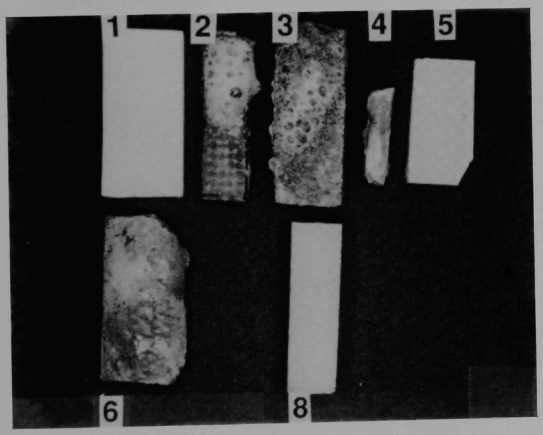

Fig. A–6. Specimens after 168–h exposure in salt II at 1000°C

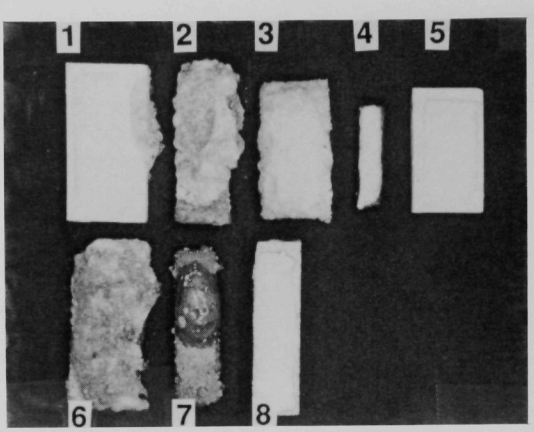

Fig. A–7. Specimens after 168–h exposure in salt II at 1200°C

Appendix B:

SEM Photomicrographs of Air-Oxidized Specimens

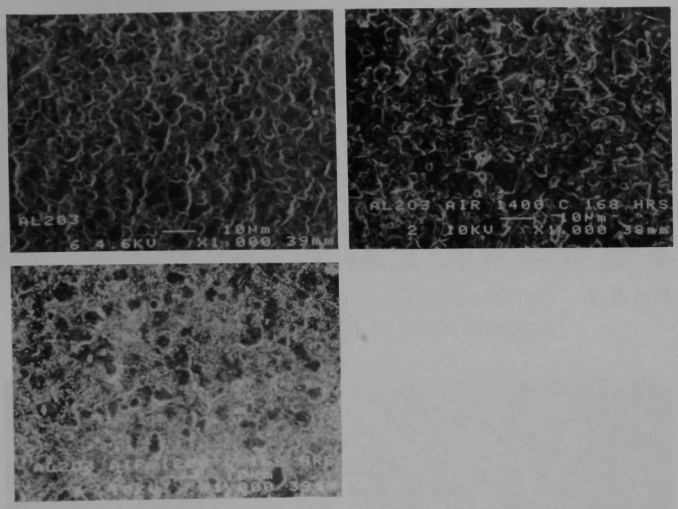

Fig. B-1. Surfaces of alumina specimens after 168–h exposure to air at 1000, 1200, and 1400°C

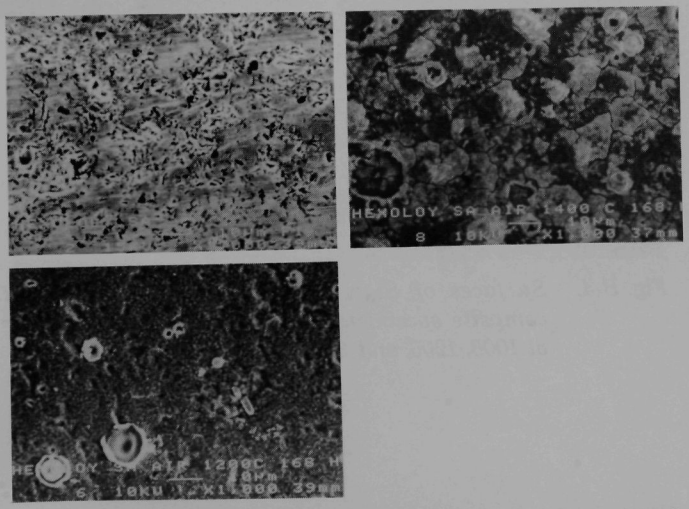

Fig. B-2. Surfaces of Hexoloy SA specimens after 168–h exposure to air at 1000, 1200, and 1400°C

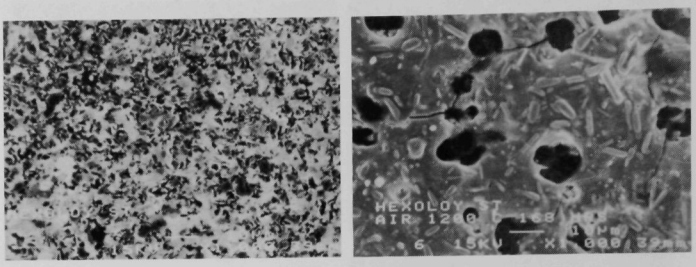

Fig. B-3. Surfaces of Hexoloy ST specimens after 168–h exposure to air at 1000 and 1200°C

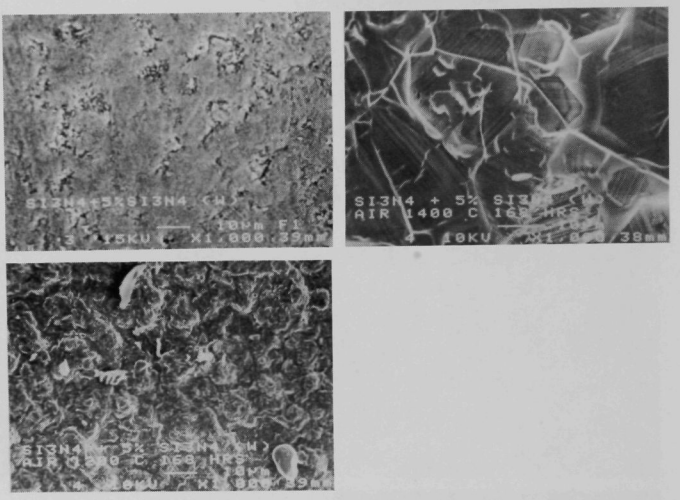

Fig. B-4. Surfaces of Si_3N_4 whiskers in Si_3N_4 matrix compsite specimens after 168 hr exposure to air at 1000, 1200, and 1400°C

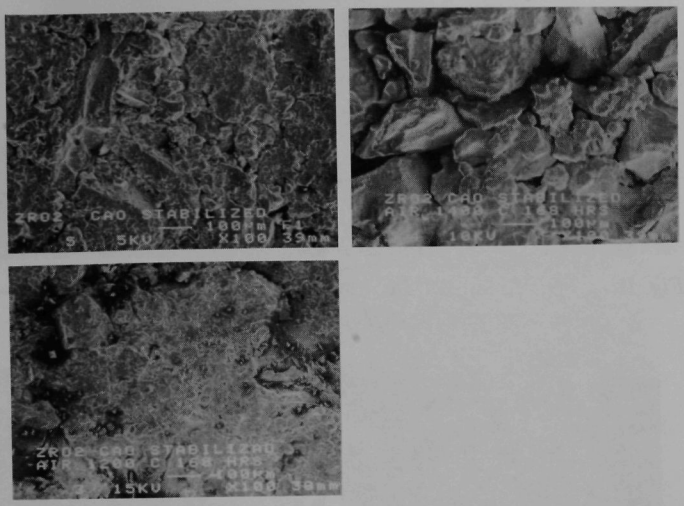

Fig. B-5. Surfaces of CaO-stabilized ZrO_2 specimens after 168–h exposure to air at 1000, 1200, and 1400°C

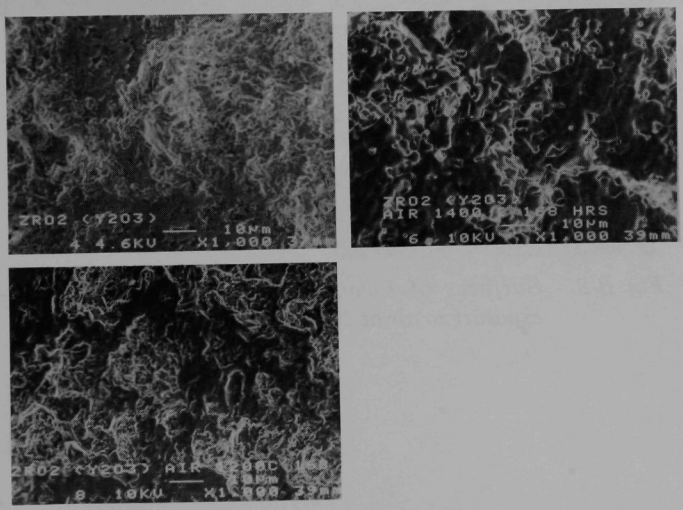

Fig. B-6. Surfaces of Y_2O_3-stabilized ZrO_2 specimens after 168 hr exposure to air at 1000, 1200, and 1400°C

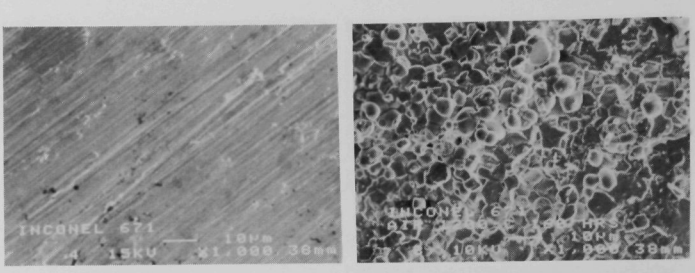

Fig. B-7. Surfaces of Inconel 671 specimens after 168–h exposure to air at 1000 and 1200°C

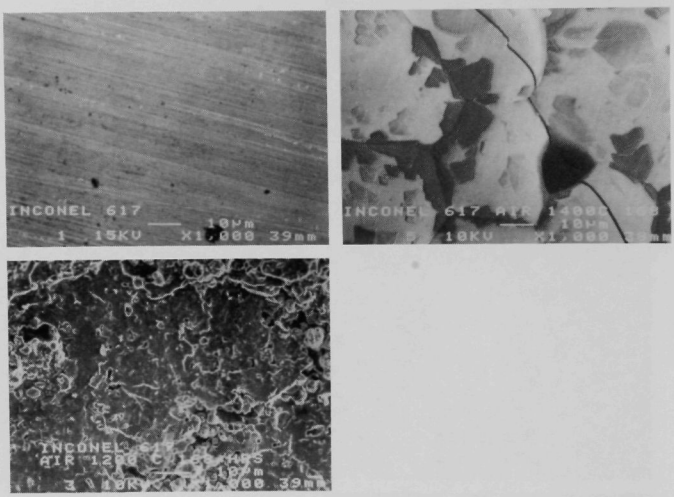

Fig. B-8. Surfaces of Inconel 617 specimens after 168–h exposure to air at 1000, 1200, and 1400°C

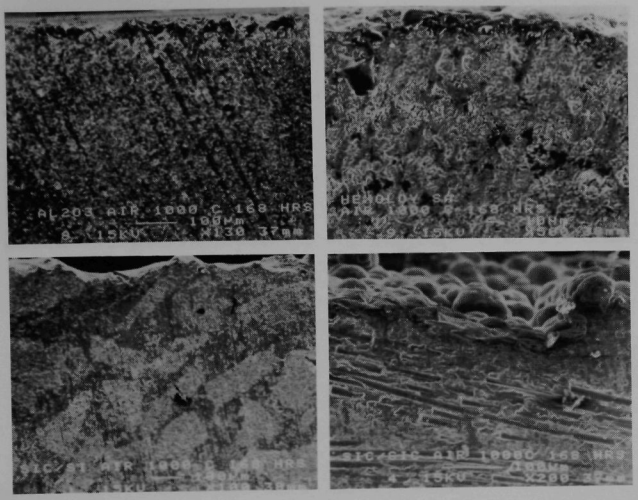

Fig. B-9. Cross sections of alumina, Hexoloy SA, SiC in Silicon matrix, SiC fibers in SiC matrix composite specimens after 168 hr exposure to air at 1000°C

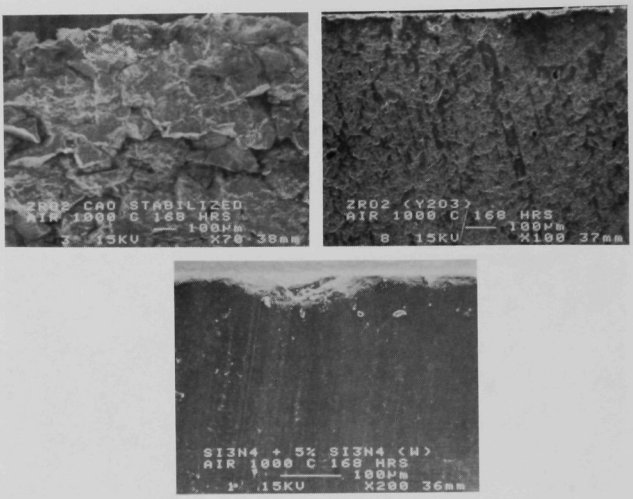

Fig. B-10. Cross sections of alumina, Hexoloy SA, SiC in Silicon matrix, SiC fibers in SiC matrix composite specimens after 168 hr exposure to air at 1000°C

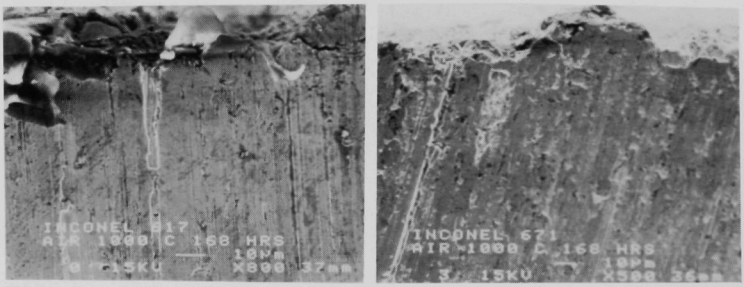

Fig. B-11. Cross sections of Inconel 617 and Inconel 671 specimens after 168–h exposure to air at 1000°C

Appendix C:

SEM Photomicrographs and EDX Analyses of Salt-Exposed Specimens

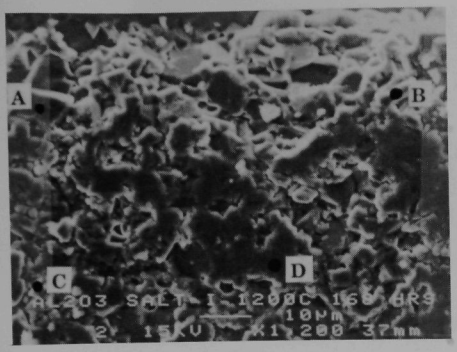

Fig. C-1
Cross section of alumina specimen after 168–h exposure to salt I at 1200°C

Alumina Sample Tested at 1200°C in Salt I

Location	Elemental Concentration (wt.%)				
	Al	Si	Na	O	S
A	72.3	-	0.3	25.1	-
B	60.9	0.3	1.0	35.2	0.4
C	72.7	-	0.7	25.6	1.0
D	79.2	-	0.6	19.5	0.7

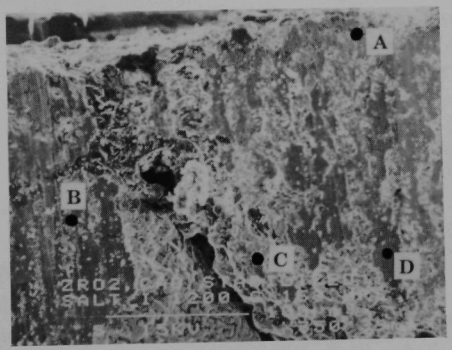

CaO stabilized ZrO_2 Sample Tested at 1200°C in Salt I

Location	Elemental Concentration (wt.%)					
	Zr	Si	Na	O	S	Other
A	62.6	1.1	13.7	3.7	5.6	Al 1.3, Ca 0.3
B	-	1.2	36.9	34.1	24.2	Ca 1.3
C	88.9	0.6	1.9	6.0	2.2	Ca 0.5
D	88.0	2.6	1.3	3.2	-	Ca 0.6, Al 0.9

Fig. C–2. Cross section of CaO-stabilized ZrO_2 specimen after 168–h exposure to salt I at 1200°C

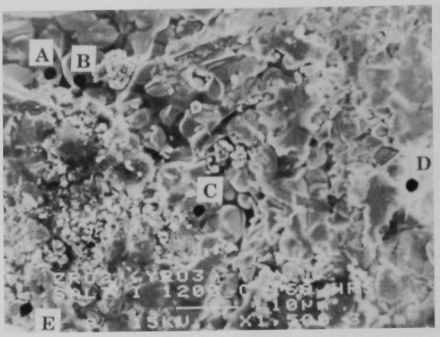

Y_2O_3 stabilized ZrO_2 Sample Tested at 1200°C in Salt I

Location	Elemental Concentration (wt.%)					
	Zr	Si	Na	O	S	Other
A	82.1	0.5	-	7.2	0.9	Y 9.3
B	77.6	0.4	0.2	9.2	0.7	Y 11.8
C	86.8	-	0.3	2.2	-	Y 10.8
D	70.5	-	0.3	10.9	0.9	Y 17.4
E	83.1	-	0.3	5.2	0.5	Y 10.9

Fig. C–3. Cross section of Y_2O_3-stabilized ZrO_2 specimen after 168–h exposure to salt I at 1200°C

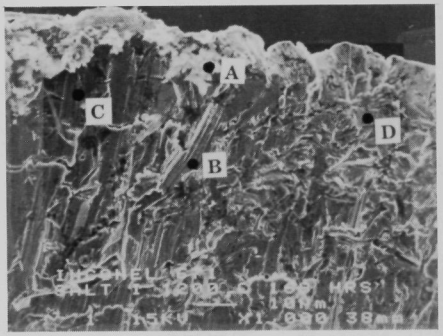

Fig. C–4
Cross section of Inconel 671 specimen after 168–h exposure to salt I at 1200°C

Inconel 671 Sample Tested at 1200°C in Salt I

Location	Elemental Concentration (wt.%)					
	Ni	Cr	Na	O	S	Other
A	4.5	4.8	5.8	6.7	1.9	Fe 69.2, Si 4.5
B	69.4	29.3	-	0.3	-	Fe 0.3
C	68.7	29.6	-	0.1	-	Fe 1.0
D	67.5	29.0	-	2.0	0.1	Fe 0.5, Si 0.7

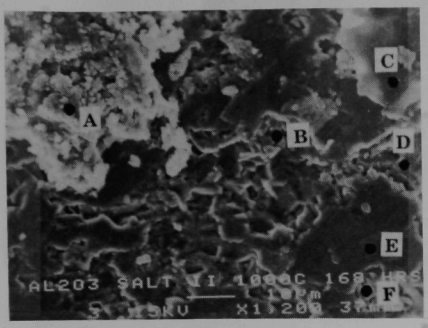

Fig. C–5
Cross section of alumina specimen after 168–h exposure to salt II at 1000°C

Alumina Sample Tested at 1000°C in Salt II

Location	Elemental Concentration (wt.%)					
	Al	Si	Na	O	S	Other
A	0.9	0.6	31.5	2.2	61.5	Ca 3.4
B	92.4	-	0.9	6.2	0.5	-
C	73.0	-	9.3	2.8	10.3	-
D	84.6	-	0.8	13.6	1.0	-
E	76.7	3.9	0.6	17.4	1.4	-
F	82.2	-	1.3	14.9	1.6	-

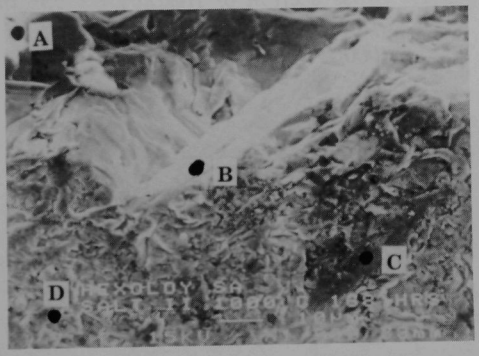

Hexoloy SA Sample Tested at 1000°C in Salt II

Location	Elemental Concentration (wt.%)					
	Al	Si	Na	O	S	Other
A	7.2	50.2	10.9	31.1	0.6	-
B	0.1	42.7	-	0.4	-	C 56.8
C	0.2	34.6	0.9	2.1	-	C 61.3
D	0.1	47.5	-	-	-	C 52.4

Fig. C–6. Cross section of alumina specimen after 168–h exposure to salt II at 1000°C

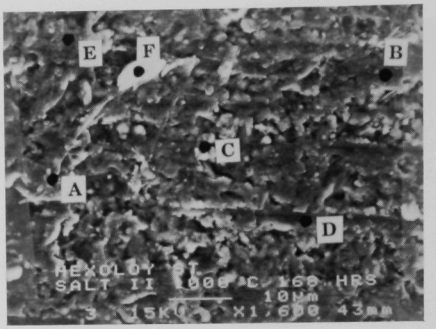

Hexoloy ST Sample Tested at 1000°C in Salt II

Location	Elemental Concentration (wt.%)					
	Ti	Si	Na	O	S	Other
A	31.6	50.0	5.8	5.5	6.4	Ca 0.6
B	1.1	97.9	-	0.2	0.5	Al 0.2
C	89.7	7.2	0.9	1.3	0.7	Al 0.2
D	1.6	97.2	-	-	1.2	-
E	3.4	59.0	17.7	0.9	18.5	Al 0.6
F	2.3	18.3	35.5	10.8	32.3	Al 0.9

Fig. C–7. Cross section of Hexoloy ST specimen after 168–h exposure to salt II at 1000°C

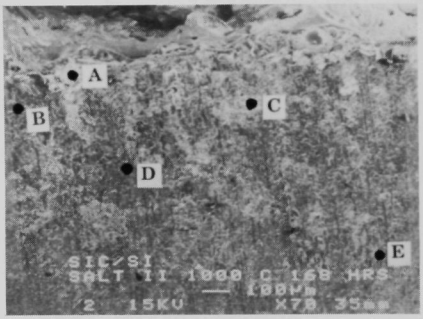

Fig. C–8
Cross section of SiC in silicon matrix specimen after 168–h exposure to salt II at 1000°C

SiC/Si Sample Tested at 1000°C in Salt II

Location	Elemental Concentration (wt.%)				
	Si	Na	O	S	Other
A	10.4	28.4	15.1	33.9	-
B	97.4	1.1	1.5	-	-
C	13.8	35.3	19.8	25.1	-
D	44.9	0.3	0.2	0.3	C 54.2
E	94.1	1.8	2.1	1.9	-

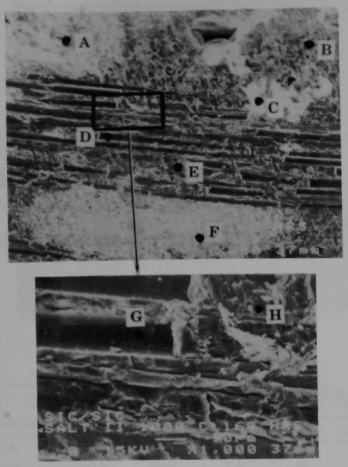

Fig. C–9
Cross section of SiC fibers in SiC matrix composite specimen after 168–h exposure to salt II at 1000°C

SiC/SiC Sample Tested at 1000°C in Salt II

Location	Elemental Concentration (wt.%)				
	Si	Na	O	S	Other
A	30.4	27.8	17.2	24.6	-
B	94.2	0.6	4.9	0.2	-
C	-	45.8	20.4	33.8	-
D	46.3	-	-	0.2	C 53.5
E	50.3	0.7	0.5	0.1	C 48.4
F	73.3	11.9	4.2	10.6	-
G	99.9	-	-	0.1	-
H	93.5	1.2	5.0	0.3	-

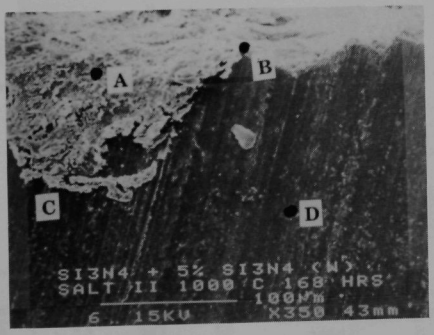

Fig. C–10
Cross section of Si_3N_4 whiskers in Si_3N_4 matrix composite specimen after 168–h exposure to salt II at 1000°C

Si_3N_4 + 5% Si_3N_4 (W) Sample Tested at 1000°C in Salt II

Location	Elemental Concentration (wt.%)					
	Al	Si	Na	O	S	Other
A	0.7	7.9	37.7	9.0	32.3	N 5.3, Mg 0.7
B	0.4	56.0	1.9	1.1	1.8	N 37.2, Mg 1.6
C	0.5	56.8	0.9	0.6	-	N 37.8, Mg 1.4
D	0.3	56.5	1.4	0.8	1.0	N 37.6, Mg 2.3

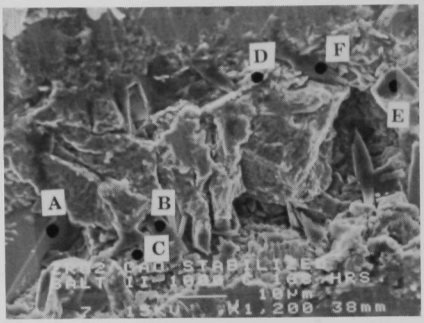

Fig. C-11
Cross section of CaO-stabilized ZrO_2 specimen after 168–h exposure to salt II at 1000°C

CaO stabilized ZrO_2 Sample Tested at 1000°C in Salt II

Location	Elemental Concentration (wt.%)					
	Zr	Si	Na	O	S	Other
A	70.9	17.1	-	9.5	2.3	Ca 0.1
B	1.4	-	22.9	14.3	41.8	Ca 19.4
C	2.0	0.4	9.1	14.5	38.6	Ca 35.4
D	88.9	0.2	1.8	3.8	4.6	Ca 0.2, Mg 0.5
E	77.6	18.6	-	2.2	1.4	Al 0.2
F	3.2	3.2	16.9	9.3	43.9	Ca 19.9, Al 2.7

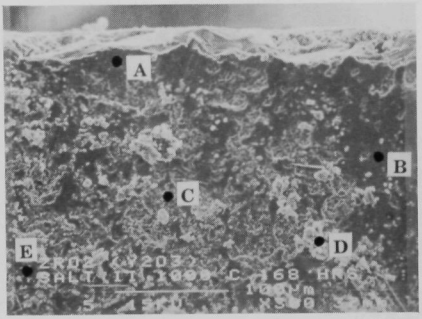

Fig. C-12
Cross section of Y_2O_3-stabilized ZrO_2 specimen after 168–h exposure to salt II at 1000°C

Y_2O_3 stabilized ZrO_2 Sample Tested at 1000°C in Salt II

Location	Elemental Concentration (wt.%)					
	Zr	Si	Na	O	S	Other
A	85.1	-	-	2.2	2.1	Y 10.6
B	82.4	-	1.7	1.6	4.0	Y 10.3
C	23.2	0.7	32.9	9.1	27.9	Y 6.1
D	-	0.3	44.1	4.7	34.4	Y 1.9, Mo 13.8
E	71.0	-	2.2	2.1	4.3	Y 20.5

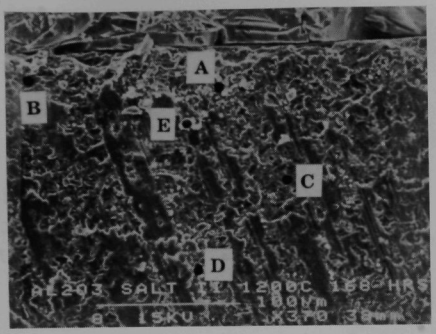

Fig. C-13
Cross section of alumina specimen after 168–h exposure to salt II at 1200°C

Alumina Sample Tested at 1200°C in Salt II

Location	Elemental Concentration (wt.%)					
	Al	Si	Na	O	S	Other
A	96.3	-	0.5	2.4	0.8	-
B	82.8	2.3	1.2	12.3	1.3	-
C	87.6	0.9	0.3	9.3	1.9	-
D	60.0	20.7	6.1	12.0	1.6	-
E	74.0	3.4	4.4	9.5	8.8	-

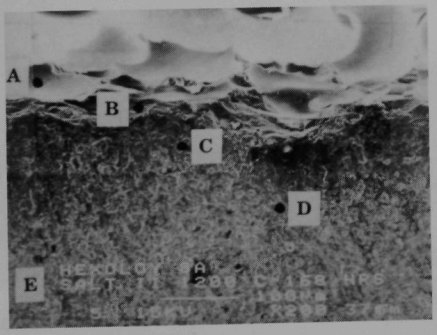

Fig. C-14
Cross section of alumina specimen after 168–h exposure to salt II at 1200°C

Hexoloy SA Sample Tested at 1200°C in Salt II

Location	Elemental Concentration (wt.%)					
	Al	Si	Na	O	S	Other
A	8.3	53.7	4.9	-	29.5	Ti 3.6
B	1.3	65.9	1.1	-	30.6	Ti 1.2
C	0.4	98.2	0.1	-	1.3	-
D	0.1	33.6	0.8	64.9	0.6	-
E	0.1	44.2	0.1	55.1	0.2	0

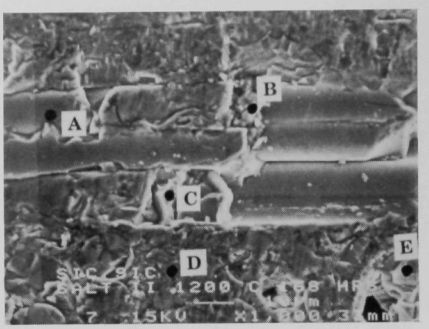

Fig. C-15
Cross section of SiC in silicon matrix specimen after 168–h exposure to salt II at 1200°C

SiC/Si Sample Tested at 1200°C in Salt II

Location	Elemental Concentration (wt.%)					
	Al	Si	Na	O	S	Other
A	13.6	53.6	8.3	24.5	-	-
B	11.9	44.8	11.1	32.2	-	-
C	0.1	46.3	-	-	-	C 53.6
D	0.2	88.3	-	-0.2	-	C 11.3

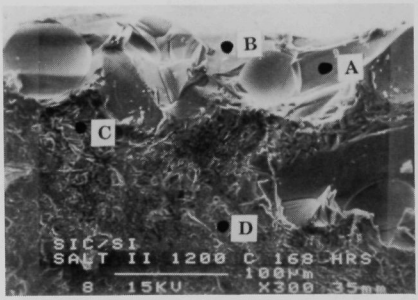

Fig. C-16
Cross section of SiC fibers in SiC matrix composite specimen after 168–h exposure to salt II at 1200°C

SiC/SiC Sample Tested at 1200°C in Salt II

Location	Elemental Concentration (wt.%)					
	Al	Si	Na	O	S	Other
A	-	97.2	-	2.8	-	-
B	2.5	15.9	-	18.2	0.7	Fe 44.4, C 14.6
C	0.4	50.1	0.3	5.6	0.5	C 43.0
D	-	99.2	-	0.3	0.2	-
E	0.2	94.8	0.8	4.1	-	-

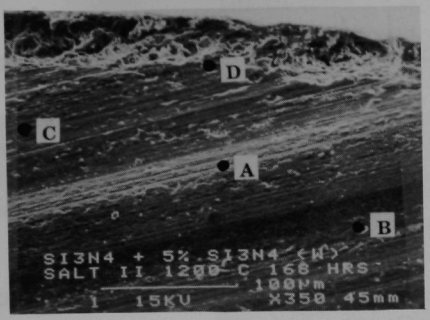

Fig. C-17
Cross section of Si_3N_4 whiskers in Si_3N_4 matrix composite specimen after 168–h exposure to salt II at 1200°C

Si_3N_4 + 5% Si_3N_4 (W) Sample Tested at 1200°C in Salt II

Location	Elemental Concentration (wt.%)					
	Al	Si	Na	O	S	Other
A	0.3	58.4	0.6	-	-	N 38.8, Mg 2.0
B	-	53.9	2.9	2.5	-	Ni 35.8, Mg 1.6
C	0.3	58.9	-	-	0.7	N 39.2, Mg 0.7
D	2.0	45.5	2.7	16.1	-	N 30.3, Mg 0.4

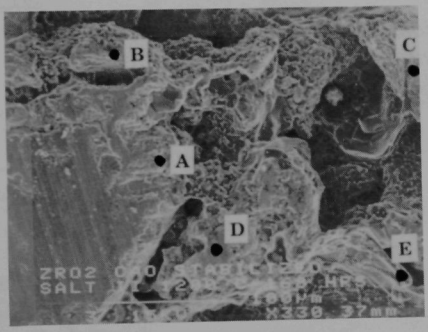

Fig. C-18
Cross section of CaO-stabilized ZrO_2 specimen after 168–h exposure to salt II at 1200°C

CaO stabilized ZrO_2 Sample Tested at 1200°C in Salt II

Location	Elemental Concentration (wt.%)					
	Zr	Si	Na	O	S	Other
A	85.5	3.3	1.7	1.3	-	Al 1.7, Ca 1.3
B	3.2	43.4	12.0	0.8	1.2	Al 20.8, Ca 18.6
C	64.8	10.9	4.4	5.6	2.2	Al 7.0, Ca 5.1
D	92.7	0.4	0.7	2.3	1.3	Al 0.2, Ca 0.4
E	-	27.6	16.9	0.8	6.0	Al 26.2, Ca 11.7

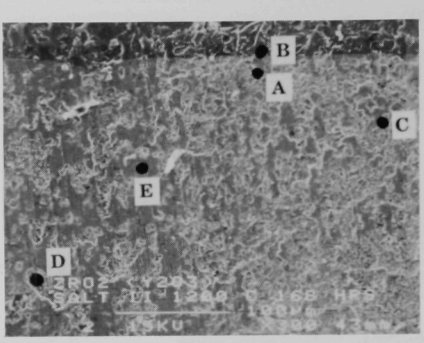

Y_2O_3 stabilized ZrO_2 Sample Tested at 1200°C in Salt II

Location	Elemental Concentration (wt.%)					
	Zr	Si	Na	O	S	Other
A	2.5	40.0	15.4	15.8	1.1	Al 21.9, Y 3.2
B	1.7	42.5	18.4	13.4	1.5	Al 22.6
C	74.0	1.3	0.6	2.4	-	Y 19.2
D	80.7	3.6	2.4	5.4	0.6	Y 5.5, Al 1.8
E	83.2	1.0	1.1	1.1	1.2	Y 12.0

Fig. C-19. Cross section of Y_2O_3-stabilized ZrO_2 specimen after 168–h exposure to salt II at 1200°C

Distribution for ANL/FE–93/1

Internal:

R. Ahluwalia
S. Borys
H. Drucker
T. F. Kassner
C. A. Malefyt
K. Natesan (10)
M. Petrick
R. B. Poeppel
D. Schmalzer
W. J. Shack
R. W. Weeks
TIS Files

External:

DOE-OSTI, for distribution per UC-114 (35)
ANL Libraries
ANL–E
ANL–W

Chicago Field Office, DOE:
Manager F. Herbaty D. L. Bray

Energy Technology Division Review Committee:

H. K. Birnbaum, University of Illinois, Urbana
R. C. Buchanan, University of Cincinnati, Cincinnati, OH
M. S. Dresselhaus, Massachusetts Institute of Technology, Cambridge, MA
B. G. Jones, University of Illinois, Urbana
C.–Y. Li, Cornell University, Ithaca, NY
S.–N. Liu, Fremont, CA
R. E. Smith, SciTech, Inc., Morrisville, NC

U.S. Department of Energy, Washington:
Office of Fossil Energy:
D. J. Beecy, S. Biondo, J. P. Carr, H. Feibus
C. W. Garrett, F. Glaser, P. Muchunas, G. Rudins
T. B. Simpson
Office of Conservation:
J. J. Brogan, A. A. Chesnes, J. J. Eberhardt
J. Eustis, E. W. Gregory II, M. E. Gunn, Jr.
Basic Energy Sciences, Materials Science Division:
J.B. Darby

DOE Morgantown Energy Technology Center:
Director J. E. Notestein

DOE Oak Ridge Operations Office:
Manager E. E. Hoffman

DOE Pittsburgh Energy Technology Center:

Director	R. Carrabetta	H. Chambers	J. D. Hickerson
M. Mathur	L. A. Ruth	C. Smith	F. W. Steffen
J. Winslow			

Oak Ridge National Laboratory:
R. R. Judkins N. Cole J. H. DeVan

Other Government - University - Industry:
S. J. Dapkunas, National Institute of Standards and Technology, Gaithersburg, MD
D. Doughty, Sandia National Laboratories
D. W. Keefer, EG&G IDAHO, Inc., Idaho National Engineering Laboratory
K. M. Prewo, United Technologies Research Center, East Hartford, CT
A. Schwarzkopf, National Science Foundation, Washington, DC
R. M. Spriggs, National Research Council, Washington, DC
I. G. Wright, Electric Power Research Institute, Palo Alto, CA
K. M. Zwilsky, National Materials Advisory Board, National Research Council, Washington, DC